National Transportation Safety Board

Office of Research and Engineering

Washington, DC 20594

RRD24FR001

MATERIALS LABORATORY

Factual Report 23-100

May 23, 2024

(This page intentionally left blank)

A. ACCIDENT INFORMATION

Location: Pueblo West, Colorado
Date: October 15, 2023
Time: 15:30 mountain daylight time
21:30 coordinated universal time
Vehicle: BNSF Coal Train Locomotive, C-ATMCRD-0-31D
Investigator: Richard Skolnekovich, RPH-10

B. COMPONENTS EXAMINED

Sections of fractured rail fragments (3)

C. EXAMINATION PARTICIPANTS

Specialist Erik Mueller, Ph.D., PE, FASM
Office of Research and Engineering – Materials Laboratory Division
NTSB, Washington, DC

D. DETAILS OF THE EXAMINATION

On October 15, 2023, a BNSF Railway train derailed near a mainline switch. The train consisted of 124 loaded hopper cars and five locomotives—two head-end and three rear distributed power units. The locomotive derailment caused 30 loaded coal hopper rail cars to depart the track on a bridge over the Interstate 25 freeway. Post-accident inspections found an area of track that had fractured prior to the derailment, based on video footage from the lead locomotive recording device (shown in Figure 1). Another piece of rail had also fractured, shown in Figure 2. Sections of the rail about this and another fractured were removed and sent to the NTSB Materials Laboratory for additional examination.

A group examination of the rail pieces for the Materials Group of NTSB investigation RRD24FR001 took place at the 5th floor and basement laboratories at NTSB headquarters in Washington, DC from Tuesday, December 12 to Wednesday, December 13, 2023. Additional metallographic examination was performed at BNSF's Technical Research & Development facility on Thursday, December 21, 2023.

Three sections of rail from the accident site had been crated and were received by the NTSB Materials Laboratory. The rail was 136 lb. that had been continuously welded and comprised Main Track 1. These sections are shown as received after removal of each shipping crate top lid cover, and represent the following sections of West Rail in Figure 3:

(a) Rail Piece #1, which was sectioned on one side and contained the 'A' side of the relatively flat fracture surface near the weld with a small fragment of Rail Piece 2, 49 inches long
(b) Rail Piece #2, with the 'B' fracture surface, which mated to 'A' along with a second jagged fracture surface 'C' on the opposite end near another weld with a small fragment of Rail Piece 3, 75 inches long
(c) Rail Piece #3, sectioned on one side with the 'D' fracture that mated to 'C', 60 inches long

Of most concern was the fracture surface near the weld at location MP 109.656, which were labeled as fracture surfaces 'A' and 'B'. The fracture was located 0.75 to 0.95 inches from the weld edge, with the weld being approximately 1.50 inches long in the longitudinal direction. This weld, shown in Figure 1 on scene, was labeled Weld #71, and it had been completed on May 29, 2023, or 4 months and 16 days prior to the accident. Figure 4 shows this fracture surface from the side opposite the weld, or 'B'. This fragment of rail (rail 2) had deformed away from its tangent (straight) direction, shown angled to the right in Figure 4.

The fractured rail pieces were sectioned 7 inches from the fracture surface on side A and 6 inches from the fracture on side B. In addition, a transverse rail section was taken on the opposite sides of the sectioning.

Figure 5 shows the mating 'A' and 'B' fracture surfaces facing the reader. The B side exhibited 'friction batter' or abrasion marks from contact with the mating fracture surface. These features were observed on the lower portion of the fracture, concentrated on the base and lower web. The streaks in the worn area were oriented vertically, consistent with up and down rubbing and movement. In contrast, the abrasion on the A side was concentrated along the upper web and head surfaces.

Figure 6 shows the A side fracture surface under oblique lighting to visually highlight fracture features. The surface was generally rough in texture with a dull, fibrous luster. The surface exhibited upward-spreading river patterns and downward pointing chevron patterns. These features were consistent with fracture originating from the base and progressing upward.

Comparing the undamaged portions of the head and web on the mating rail fracture in Figure 7 shows comparable features in the same orientation, consistent with fracture progressing upward from the web through the head. These features were consistent with fracture progressing from the base of the rail, which exhibited post-fracture damage.

Figure 8 and Figure 9 show the mating A and B fracture surfaces from the field and gage sides, respectively. These fractures were oriented vertically, with a convex shape toward the middle of the web. The fracture was not located along the weld, but rather

0.75 inches outside the weld filler boundary within rail 2. On the field side of the web, there was a wavy longitudinal witness mark approximately 2 inches about the base. The gage side of the rail 2 portion also exhibited wear along the web angled toward the gage side, located on the fracture section of the rail with the weld.

Figure 10 shows the running surface of the head about the fracture. The side of the fractured rail opposite the weld (labeled 'B' in the figure) exhibited downward oriented deformation, which can also be seen in the left in Figure 5. According to the labeling on the rail, the running direction of the derailed train was left to right in Figure 10. There were indications of shelling on the gage side of rail 2 on the left in the figure—these features were absent on the opposite side of the weld (the right rail 1 in Figure 10).

Figure 11 shows an angled view of the underside of the base from field side. This demonstrates the degree of weld filler and flash present below the base.[1] The flash thickness was approximately 0.30 inches at maximum. There was also a small piece of the base that had fractured and was missing from the 'B' side of the fracture.

Figure 12 shows an angled view of the 'A' side fracture surface at the base, illustrating the initiation region of the fracture surface. This area was sectioned and excised for additional examination. Figure 13 shows a montage of the fracture surface section near the base after cleaning in an ultrasonic bath with acetone. The fracture surface exhibited two larger, angled river marks emanating from the underlying layer of flash.

While most of the fracture surface exhibited dull, fibrous qualities, a thumbnail shaped area was present along the initiation region with flatter features and a more reflective luster (Figure 13). The boundaries of this region are annotated in Figure 14, and they exhibited crack arrest marks, consistent with an initial progressive crack. This crack also exhibited ratchet marks, consistent with multiple crack initiation sites, as annotated in Figure 15. These initiation sites were located along the boundary between the rail base and the underlying flash.

This section of the fracture surface was examined using a field emission scanning electron microscope (SEM). The locations of the figures from SEM examination are shown on Figure 15. Figure 16, Figure 17, and Figure 18 show a typical area towards the end of the initial crack. As illustrated in these figures, the crack area exhibited fatigue striations, consistent with fatigue crack propagation. Outside of the fatigue thumbnail crack, the fracture surface exhibited cleavage facets and dimpled rupture, consistent with subsequent overstress fracture. These features are demonstrated in Figure 19.

[1] Flash, also described as fins or finning, is any unwanted and excess material attached to a solidified metal caused by an imperfect mold or die, which for welds is when some liquid metal leaves the weld joint and forms around the weld.

Examination of the crack initiation sites found areas with gaps, voids, and nonmetallic material. Figure 20 shows one initiation site, which exhibited an inward-oriented gap. Above this initiation site, fine striations were present, oriented consistent with crack propagation upward and outward in the figure.

Both mating sides of the 'A' and 'B' fracture surfaces were bisected along the longitudinal centerline. These sections were ground, polished, hardness tested and then etched at BNSF facilities in Topeka, KS. The outer faces of one of the sections through the weld is illustrated in Figure 21. Figure 22 shows a closer angled view of the cross section through the base. The weld itself did not exhibit macroscopic indications of porosity or slag inclusions.

However, on the fringes of the weld boundary along the base were areas of smaller longitudinally-oriented gaps, shown in Figure 22. Figure 23 shows an angled view of the edge with the crack initiation site. A microscopic gap was present along the edge with the fracture.

Figure 24 and Figure 25 show the 'C' side of the second fracture surface. This surface and the mating 'D' surface exhibited a zigzag shaped jagged morphology. Part of the head portion of the fracture surface was angled toward the field side, with some of the web angled towards the gage side. As shown in Figure 25 and Figure 26, the web and base portion of the fracture extended longitudinally along the web, with the fracture upwards along the head appearing as intersecting.

Figure 27 shows a top-down view of this fractured side of rail with the head fragment positioned as found on-scene, and Figure 28 shows the fractured head section placed to the side. Figure 29 shows the 'C' side with the sections in place at the time of fracture. All these fracture surfaces exhibited a dull luster with a rough texture, consistent with overstress fracture through rail steel. There were no indications of thumbnail cracks or features consistent with other fracture modes on these surfaces.

The fracture pattern at the on-scene portion of the examination for 'C' and 'D' showed crack branching as the fracture proceeded upward from the base (see Figure 2). This fracture pattern was consistent with the primary fracture along the base and web, with the secondary fracture front proceeding upward through the head.

Transverse cross sections through the rail were taken away from the 'A' and 'B' fracture from both the newer rail 1 and the older rail 2. These sections, shown in Figure 30, were used to help compare the rail profile to an ideal new profile for 136 lbs. rail. In addition, a MiniProf rail head profilometer was used to measure the geometry of the heads and running surface of both rails' heads away from the fracture surface.

Figure 31 shows the rail profiles of both the rail 1 (from the 'A' side) and rail 2 (from the 'B' side) superimposed on each other. Figure 32 shows these same profiles compared with an ideal new 136 lbs. rail profile. These demonstrate that rail 1 profile was closer to that of a new rail, whereas the older rail 2 had worn enough to create a difference in head height. This difference was 0.1742 inches between each rail, and a difference of 0.1720 inches from the ideal new profile for rail 1.

The 'A' and 'B' fracture surfaces were sectioned longitudinally along the centerline to extract flat specimens for macroscopic metallographic examination. These sections and their locations are detailed in Figure 33 through Figure 35. These sections were ground, polished, and etched with a warm hydrochloric acid solution for 15 minutes at the BNSF Technical Research & Development facility in Topeka, KS.

Figure 36 shows the longitudinal sections across the fracture surface and adjacent weld, after etching. Figure 37 shows the same image but annotated to show the different regions revealed from the etching process. The figures clearly show the weld filler region, which exhibited a finer grain structure than the surrounding rail microstructures. The rail exhibited coarser grains, articulated by the mottled appearance.

The surrounding heat affected zone (HAZ) was bounded by a bluish halo, as denoted in Figure 37. The fracture and the crack initiation site were outside, though adjacent to, the weld filler. The fracture was within the HAZ on the rail 2 side, except for the small region on the top near the head, denoted by the white arrows on the top of Figure 39 in that location. The white arrows on the bottom denote the space between the weld filler and initiation site to the right of the fracture.

The thermite weld manufacturer, Orgo-Thermit, Inc., lists several dimensions corresponding to various required thicknesses of the weld filler and heat affected zones at various heights.[2] These are illustrated in Figure 38 as measurements A through H. These measurements are detailed in Table I. Additional measurements are shown in Figure 39, including head to base measurements and distances of the fracture to the filler and HAZ boundaries. None of the measurements of the weld or the surrounding HAZ were outside the requirements prescribed welding procedure.

After grinding and polishing, but prior to the etching procedure, hardness testing was performed per ASTM E18. The indentations were taken both longitudinally across both sections of rail, and transverse on rail A from base to head. These data were plotted in Figure 40 and Figure 41 in HRC. The longitudinal hardness data, taken 5 mm (0.20 inches) from the head surface, averaged 36 HRC in Rail A and 41 HRC in Rail B.

[2] Orgo-Thermit is a manufacturer and supplier of rail welding materials, located in Manchester, NJ.

The hardness of both rails dropped at the interface with the HAZ, rising again to around 35 HRC in the weld filler. The lowest hardness data point was 27 HRC in the HAZ of Rail B. The required weld filler hardness range from the AREMA specification is 290-350 HB, or 29-38 HRC.[3] The transverse hardness averaged 33 HRC, as shown in Figure 41. The hardness was about 1 HRC higher in the head region, with the highest data point being 36 HRC. These hardness data were consistent with rail 2 ('B' fracture surface side) being classified as 'standard' rail, and rail 1 ('A' fracture surface side) being classified as 'head-hardened' rail.

Figure 42 shows a closer view of the etched specimen where the fracture intersected the head. This was the only portion of the fracture that extended into the weld filler. This area also demonstrated the post-fracture head deformation of Rail B on the left, which exhibited downward deformation and grain flow.

Figure 43 shows a closer view of the fracture surface near the base and the edge of the weld filler. Figure 44 shows a closer view of the area, with a porous region located below the initiation site, consistent with weld flash. This flash was located below a small crack facing the weld filler, illustrated in Figure 45. The flash contained several discolored, nonmetallic inclusions, consistent with remnants of the mold. Figure 46 shows an annotated view of several of these measurements, with the aforementioned crack between the flash and base being 0.025 inches long in this location.

Figure 47 shows a holistic view of the base and flash at the weld filler on the opposite ('A') side of the fracture. The interface between the weld filler and the HAZ on the intact side also exhibited cracking near the base, as shown in Figure 48. This crack extended 0.036 inches between the flash and the base from an initial area of entrained material 0.008 inches at the corner. This crack was 0.034 inches from the bottom of the flash surface.

Additional sections of the base near the fracture surface and side opposite weld were excised, as illustrated in Figure 49. These areas were mounted and polished and examined in both the as-polished and etched conditions, after etching with 2% Nital. Figure 50 shows the corner of the weld filler with the HAZ from the rail 2 side (faces the fracture surface 'A'). The opposite rail 1 corner with the weld filler is shown in Figure 51. This figure shows an area of flash underneath the base of rail 1 outside the weld area. This flash constituted a gap and crack underneath the base of this section of rail.

Figure 52 shows a cross section through the fracture surface 'A' between the rail 1 HAZ and the weld flash underneath the base. As shown in Figure 53, there was some contrast between the flash and the rail, in addition to several pores along the

[3] "2.1. Specifications for Steel Rails." *AREMA Manual for Railway Engineering*. American Railway Engineering and Maintenance-of-Way Association: Lanham, MD (2016)

boundary between the two areas. As seen in Figure 53, several microcracks had propagated from the largest of the pores.

Figure 54 shows the same area in the etched condition, illustrating the differences in microstructure between the rail HAZ, flash below the base, and the weld filler on the leftmost part of the figure. The boundary manifest as a whiter-etched line, where the pores and cracks were located. While smaller, these pores continued to be present further along the boundary, as shown in Figure 55.

Most of the flash exhibited pores and entrained nonmetallic material, as shown in Figure 56. While some of these pores were large, smaller pores were present along the interdendritic areas of the region.

Several areas of the microstructure were also examined near the weld and 'A' fracture surface. Figure 57 shows a typical microstructure of an area of rail 2 outside the heat affected zone. This microstructure showed a mixture of pearlite, bainite, martensite and other constituents. There were also longitudinally-oriented elongated gray-colored phases, consistent with manganese sulfide (MnS) stringers typical of this composition.

In the heat affected zone, the microstructure exhibited more pearlite with coarser features. This contrasted with the finer grains of the weld filler, as shown at the interface between the HAZ of rail 2 and the weld material (Figure 58).

Figure 59 shows a typical area of the weld filler, showing finer grain size, along with a distribution of darker spherical features, consistent with pores from gas entrapped during solidification. Figure 60 shows a closer view of this area, showing the spherical pores along the prior austenite grain boundaries. There was also lighter-colored ferrite in the pearlite colonies, consistent with a lower carbon content in the weld material. Areas of the weld filler closer to the base/flash interface exhibited larger and more tortuous porosity, illustrated in Figure 61 and Figure 62. This porosity was consistent with shrinkage porosity that formed due to a lack of liquid to fill areas during solidification and shrinkage.

Sections of rail A, rail B, and the weld filler were sent to a third-party laboratory to determine the chemical composition of each.[4] The testing, performed at NSL Analytical, found the data listed in Table II and Table III. The data for each rail were consistent with the AREMA specification for carbon steel. The weld filler chemistry data reported were also within specification limits for the AREMA limits for post weld compositions. The hydrogen content of each rail was also examined and was found to be less than 1 ppm for each rail piece.

[4] Chemical testing was performed by NSL Analytical Services, Inc., headquartered in Cleveland, OH.

The surface features were consistent with fracture of rail 2 in the heat-affected zone near a weld. This fracture was due to a fatigue crack that initiated from at the boundary between the rail base and weld flash that solidified underneath the part. The fatigue crack propagated into the rail base until the applied stresses in this area exceeded the tensile strength of the rail, leading to overstress fracture.

Submitted by:

Erik M. Mueller
Materials Research Engineer

Table I. Various measurements of the longitudinal weld and heat affected zone (HAZ) cross section in Figure 38.

Measurement Location	Required Width (in)	Measured Width (in)
A - Head width	1.7716	3.319
B - Near head width	1.5748	2.05
C - Mid width	1.5748	2.184
D - Near base width	1.5748	1.731
E - Base width	1.5748	2.299
F - Top HAZ width		4.969
G - Mid HAZ width		4.12
H - Base HAZ width		4.11

Table II. Chemical compositions of Rail 1 and Rail 2 contrasted with AREMA Specification for carbon rail steel (Section 2.1, Table 4-2-1-3-1a).[3]

Element	Spec. Minimum	Spec. Maximum	Rail 1 (wt. %)	Rail 2 (wt. %)	Method
Fe			97.236	97.397	Balance
Mn	0.75	1.25	1.00	1.00	ICP
C	0.74	0.86	0.82	0.75	LECO Furnace
Si	0.10	0.60	0.28	0.29	ICP-MS
Cr		0.30	0.27	0.22	ICP-MS
Ni		0.25	0.091	0.084	ICP-MS
Mo		0.060	0.021	0.017	ICP-MS
S		0.020	0.010	0.008	LECO Furnace
P		0.020	0.009	0.010	ICP-MS
V		0.010	0.002	0.002	ICP-MS
Al		0.010	0.001	0.002	ICP-MS
H			<1 ppm	<1 ppm	ICP-MS
Cu			0.26	0.22	ICP-MS

Table III. Chemical compositions of the weld filler contrasted with AREMA Specification for post weld chemistry limits (Table 4-3-18).[3]

Element	Spec. Minimum	Spec. Maximum	Weld Filler	Method
Fe			97.85	Balance
Mn	0.50	1.40	0.67	ICP
C	0.50	0.85	Not reported	LECO Furnace
Si	0.20	1.40	1.15	ICP-MS
Cr		0.80	0.072	ICP-MS
Cu		0.20	0.068	ICP-MS
Ni		0.10	0.031	ICP-MS
Mo		0.10	0.007	ICP-MS
S		0.035	Not reported	LECO Furnace
P		0.040	Not reported	ICP-MS
V		0.45	0.078	ICP-MS
Al		0.65	0.086	ICP-MS
W			0.008	ICP-MS
Sn		0.02	0.003	ICP-MS
Co			0.006	ICP-MS
Ti		0.05	0.003	ICP-MS
Ge			0.002	ICP-MS
Nb			0.001	ICP-MS

Figure 1. Photograph of the initial broken rail at M.P. 109.656 located on the left stock rail, viewed from the gage side. Weld #71 was completed on May 29, 2023 (Courtesy NTSB-RPH).

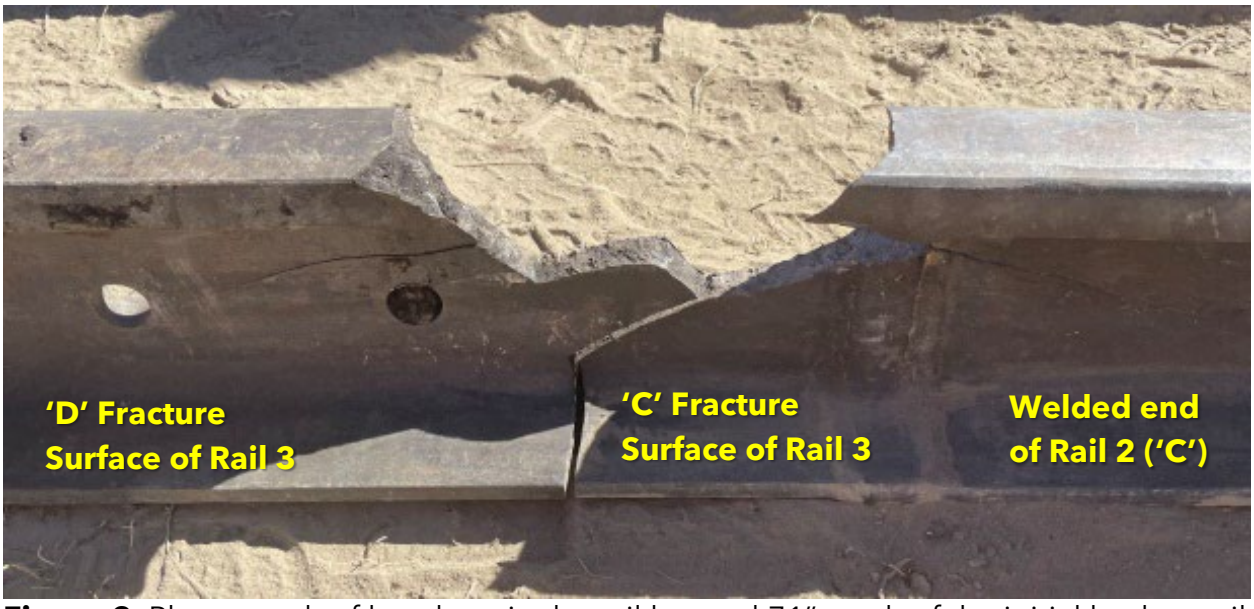

Figure 2. Photograph of breakout in the rail located 71" north of the initial broken rail (weld #71), viewed from the field side (Courtesy NTSB-RPH).

Figure 3. The sections of rail, as received in crated condition by the NTSB Materials Laboratory. The pieces are (a) Rail Piece 1, which the 'A' fracture and the opposite sectioned surface, (b) Rail Piece 2, with the 'B' and 'C' fracture surfaces, and (c) Rail Piece 3 with the 'D' fracture surface and a sectioned end.

Figure 4. View of Rail fragment #2, showing the 'B' side of the fracture surface that mated with surface 'A', and the right ward bend in the rail, with the 'C' at the opposite end.

Figure 5. The mating fracture surfaces near the weld of rail at MP 109.656, showing the upstream (left) and downstream (right) sides.

Figure 6. Oblique lighting view of the downstream fracture surface 'A', showing ratchet marks and chevron features emanating from the bottom of the base.

Figure 7. The mating upstream side of the rail fracture surface 'B', showing abrasion and vertical rubbing in the base, with downward oriented chevron marks on the web and head.

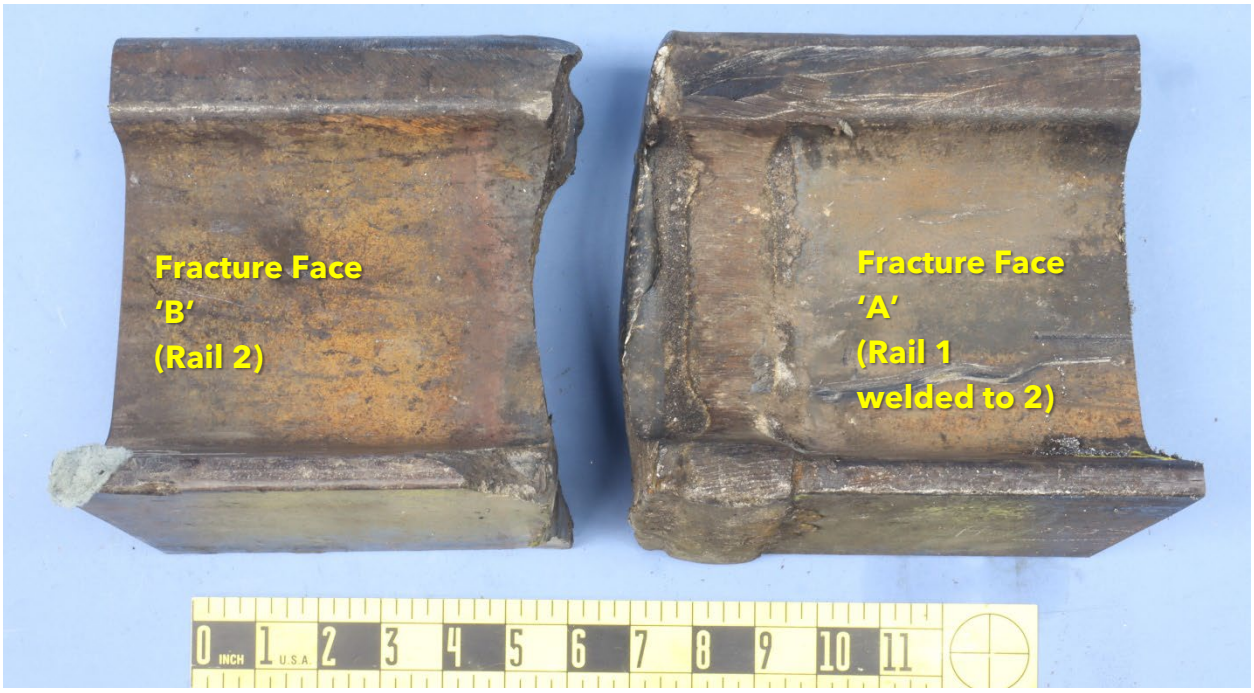

Figure 8. Field side views of the rail sections about the fracture.

Figure 9. Gage side views of the rail sections about the fracture.

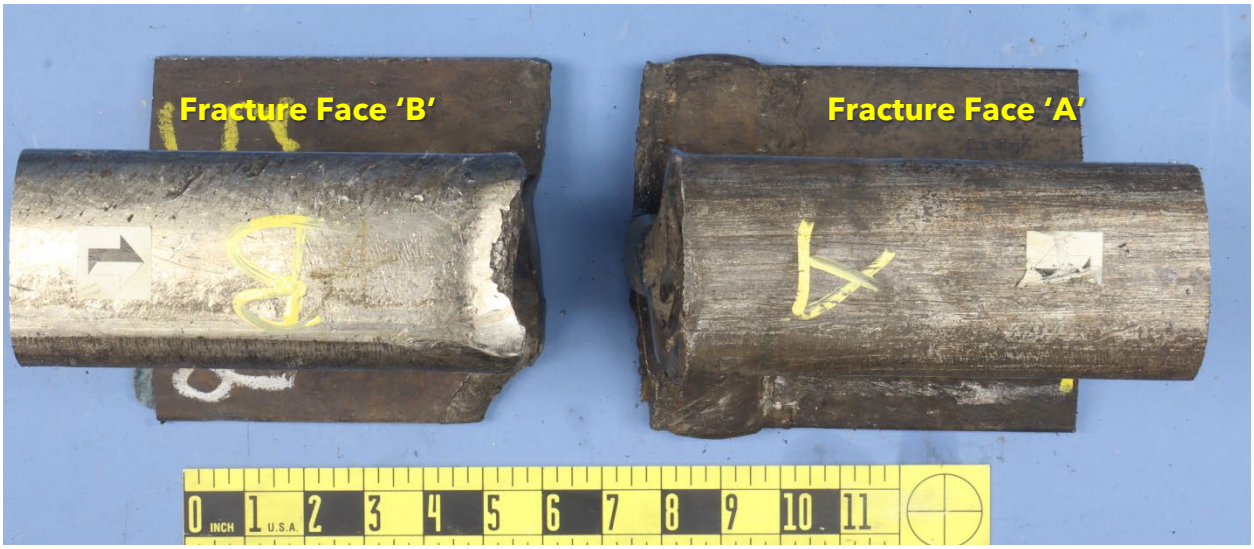

Figure 10. View of the fractured rail sections from the head running surface, with the train running direction labeled.

Figure 11. Angled view of the base underside from the field side of the fractured rail.

Figure 12. Angled view of the fracture initiation area of the downstream rail fracture 'A'.

Figure 13. View of the fracture initiation area after sectioning from the downstream rail face 'A'.

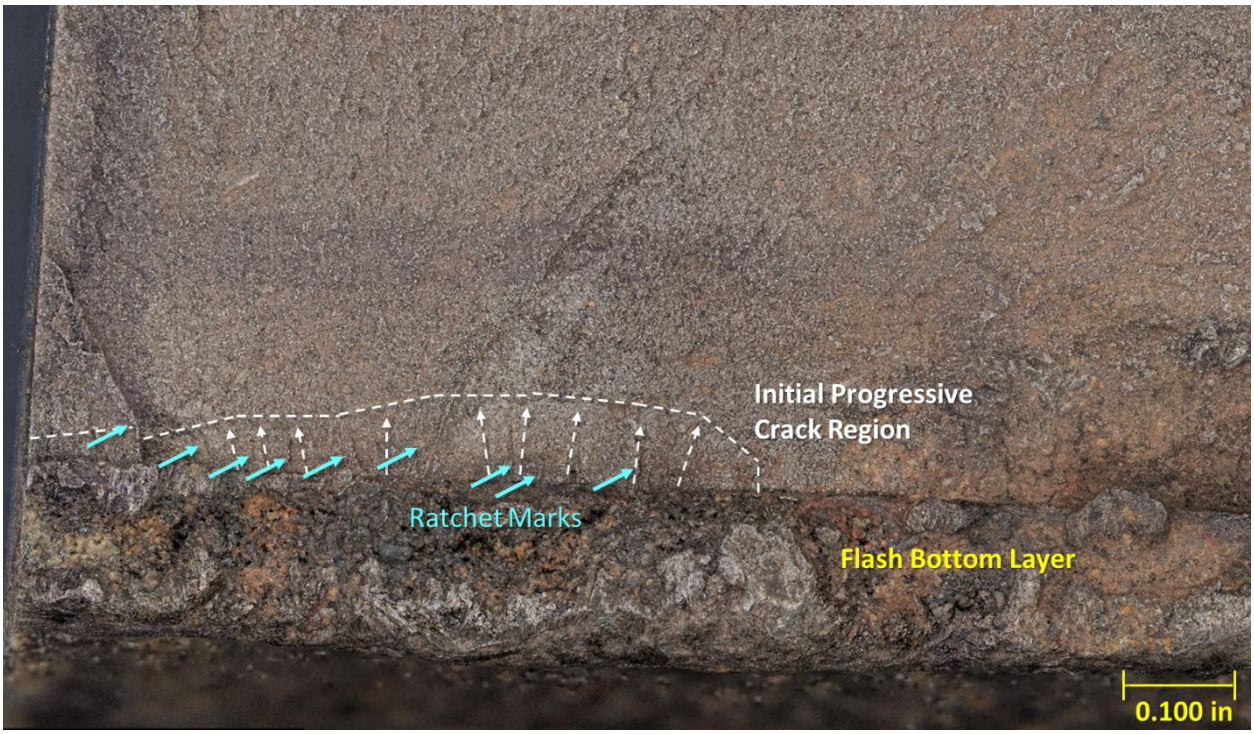

Figure 14. Annotated view of the boundary of cracking with arrest marks and ratchet marks.

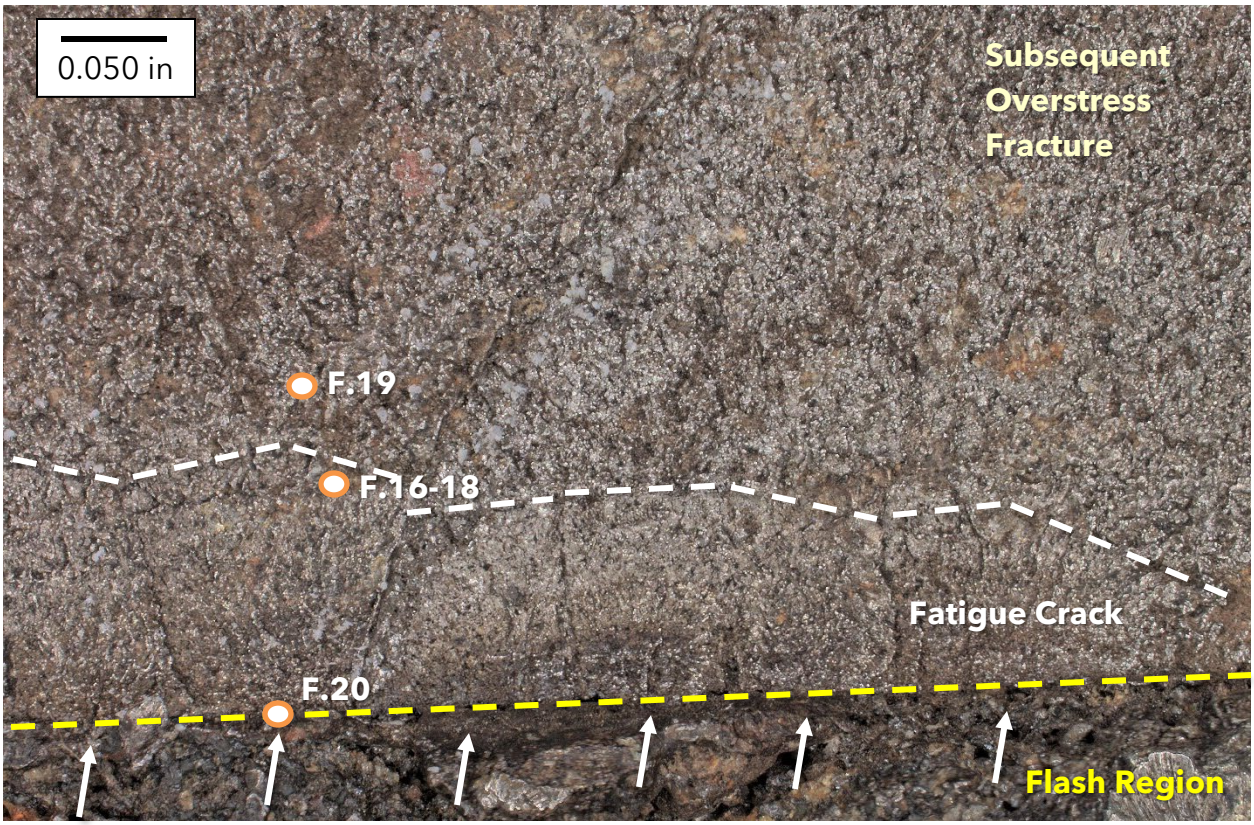

Figure 15. Closer view of some of the crack initiation sites along the boundary with the flash layer below the base, annotated to show locations of later **Figure 16** to **Figure 20**. The white arrows represent individual crack initiation sites.

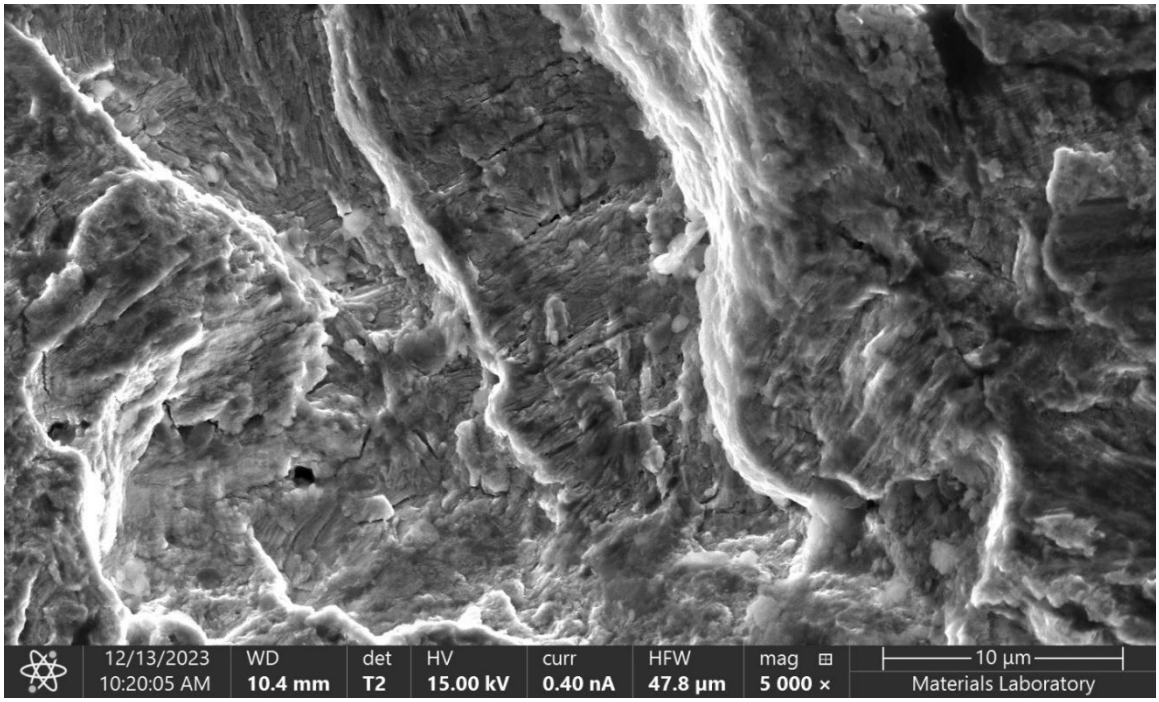

Figure 16. Secondary electron (SE) micrograph of a typical area near the end of the crack in **Figure 15**.

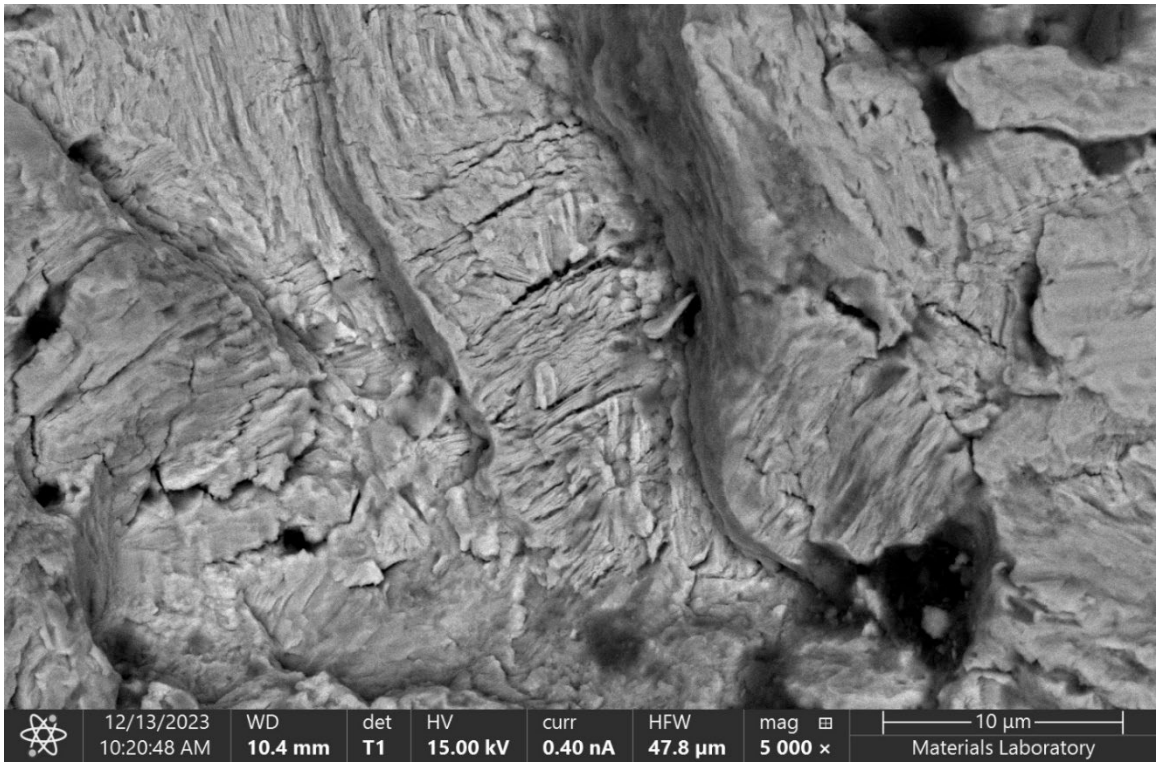

Figure 17. Backscattered electron (BE) micrograph of the area in **Figure 16** showing distinct fatigue striations.

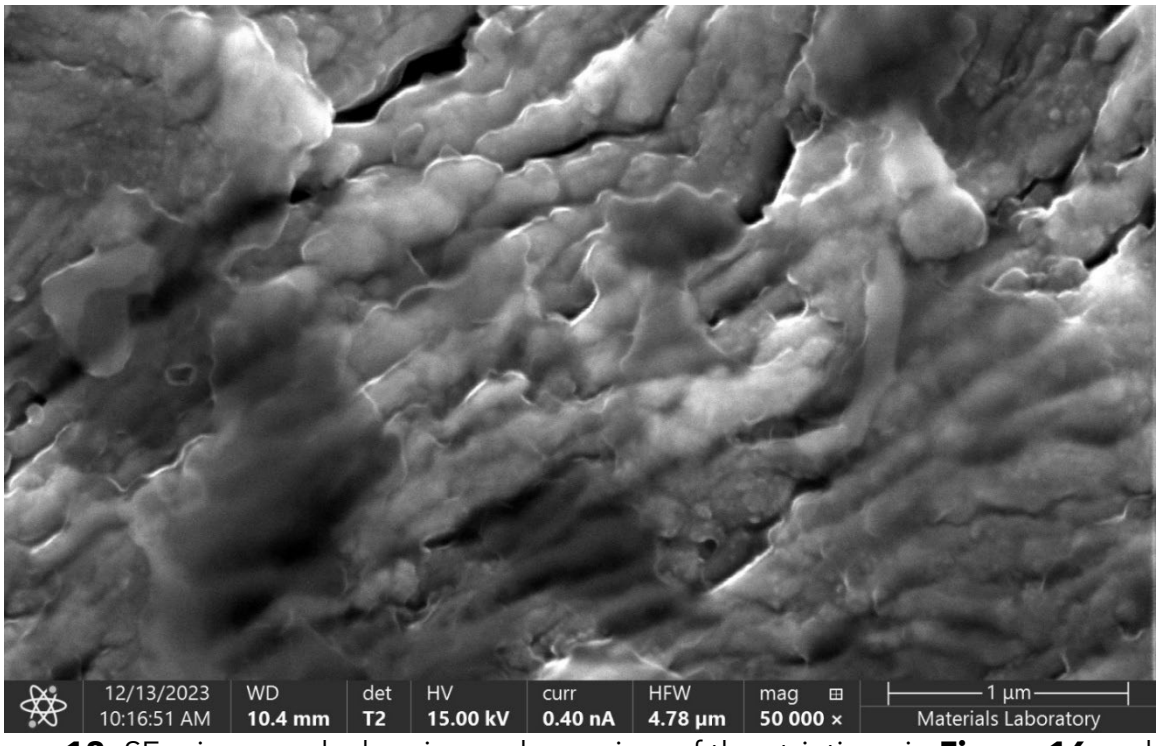

Figure 18. SE micrograph showing a closer view of the striations in **Figure 16** and **Figure 17**.

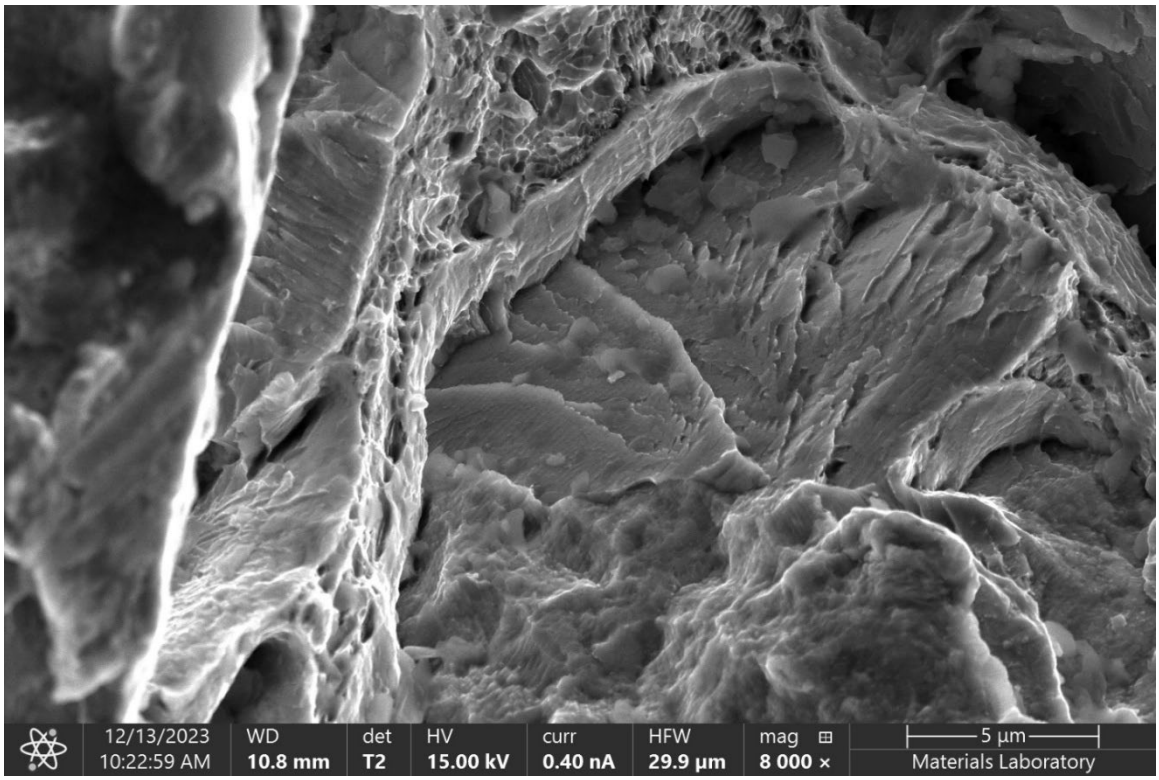

Figure 19. SE micrograph of a typical area of the fracture outside the fatigue crack, showing dimpled rupture and cleavage facets.

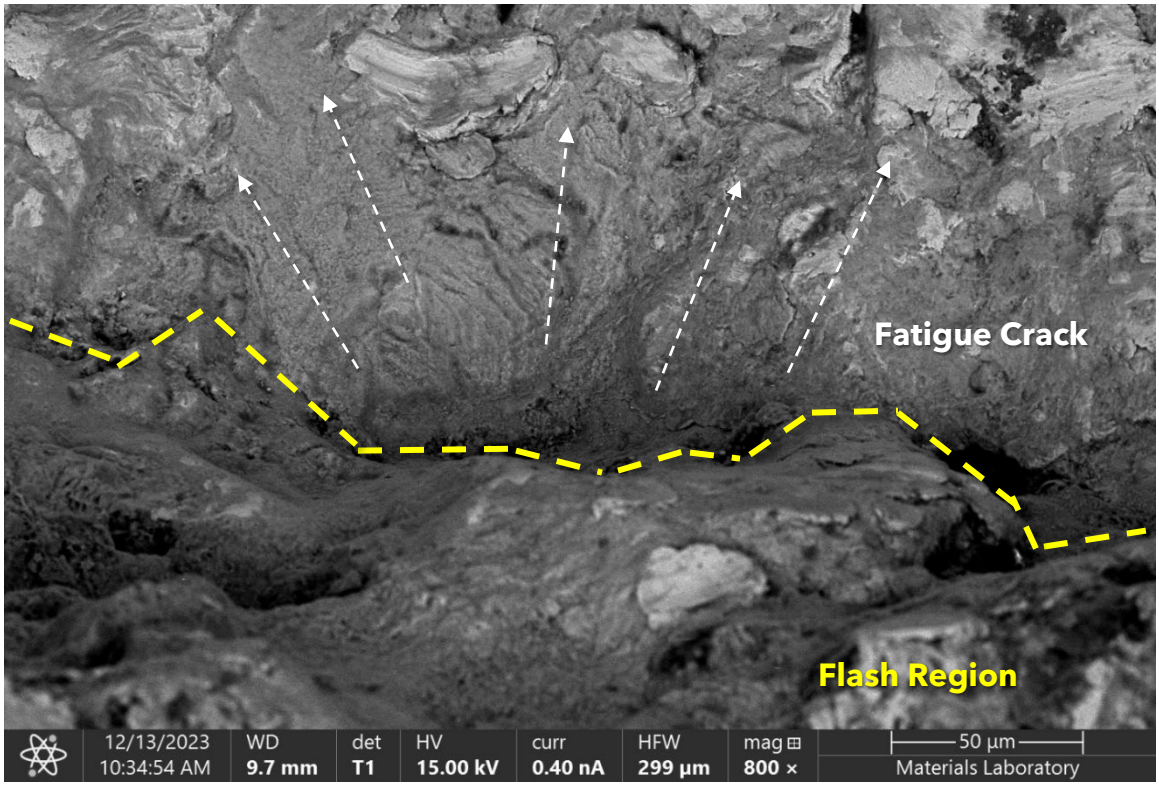

Figure 20. BE micrograph of a fatigue crack initiation site along the flash/base boundary with arrows representing initial crack growth directions from initiation.

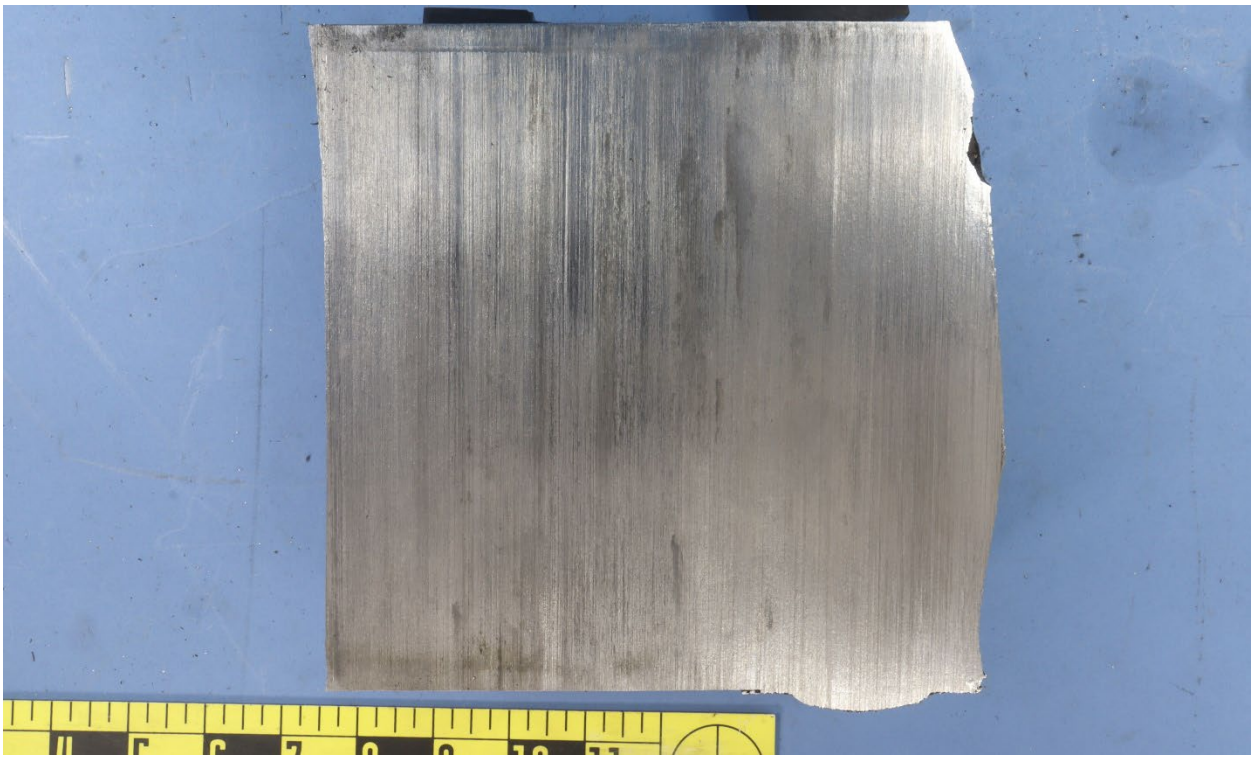

Figure 21. Cross section through the middle of the downstream rails 1 and 2 through fracture surface 'A'.

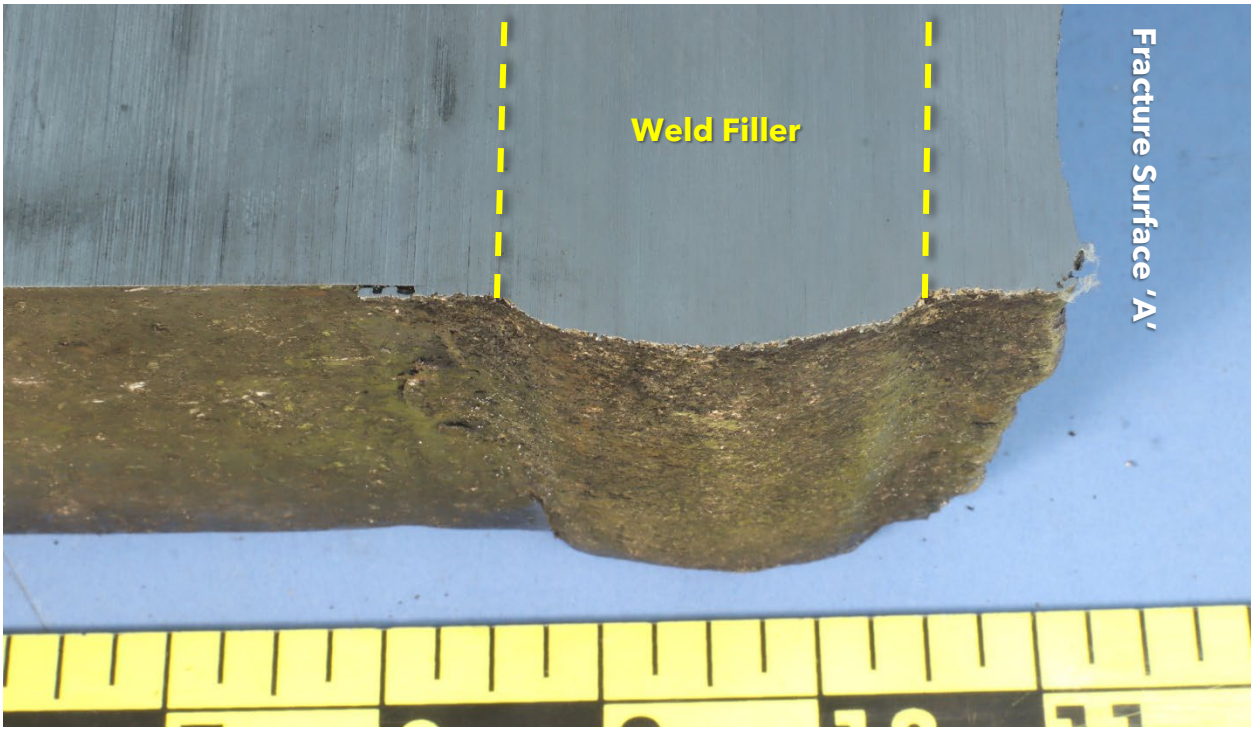

Figure 22. Angled view of the cross section through the weld along the base.

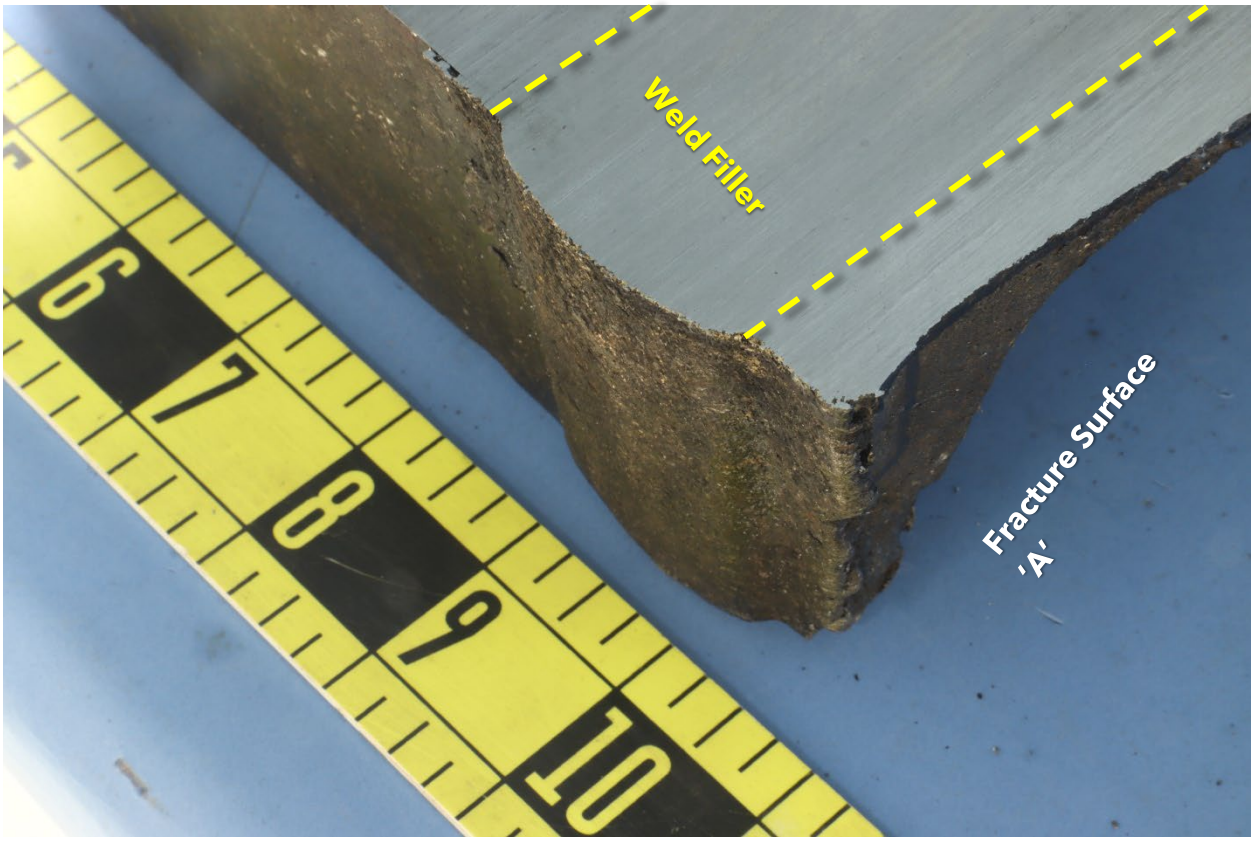

Figure 23. Corner view of the fracture surface, base surface, and longitudinal cross section of the downstream rail.

Figure 24. View of the second fracture surface through rail 3, showing from fracture surface 'C'.

Figure 25. View of the second fracture surface 'C' from the field side, showing the fracture through the rail 3 piece (right) welded to rail 2 (left).

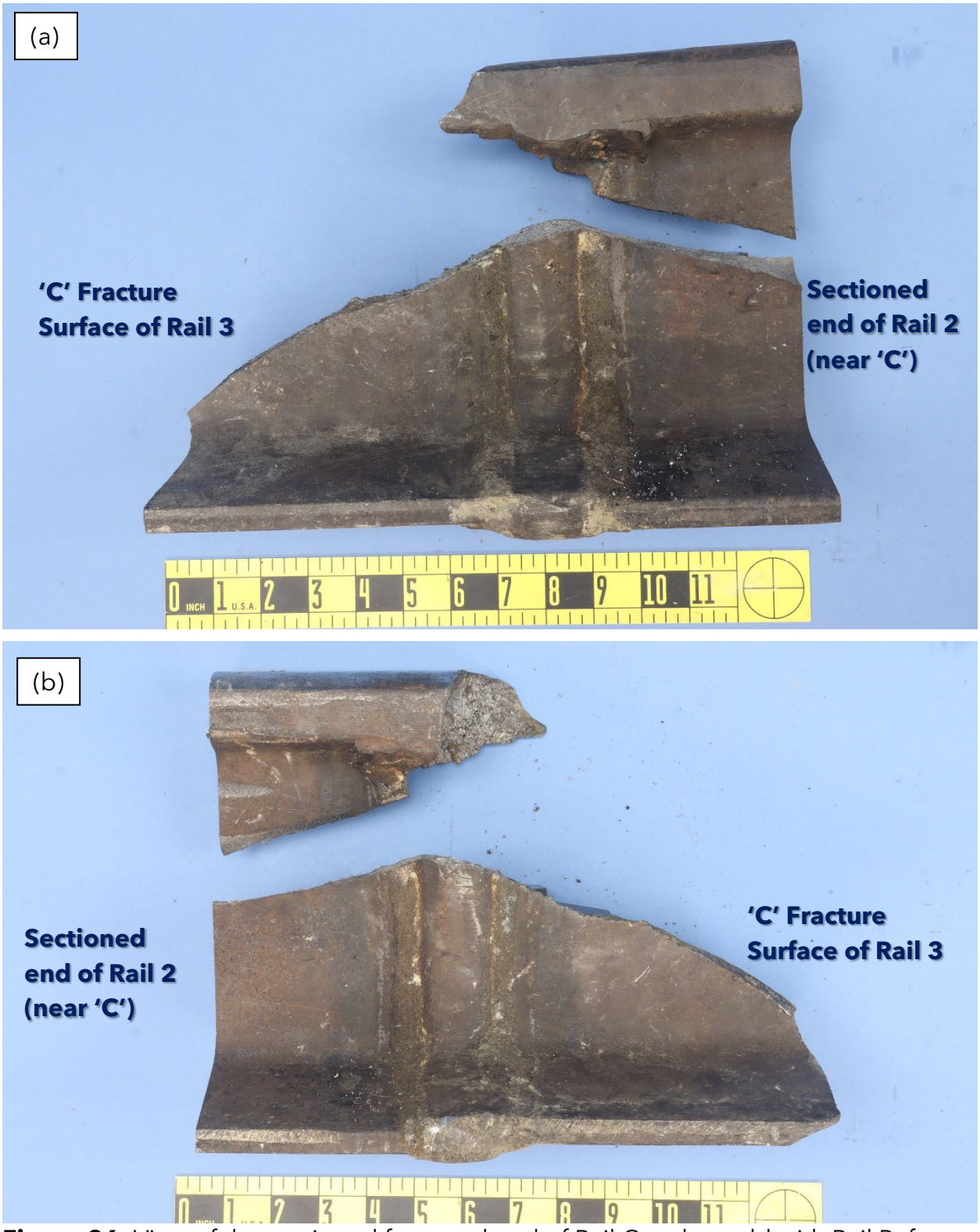

Figure 26. View of the sectioned fractured end of Rail C at the weld with Rail B, from (a) the gage side and (b) the field side.

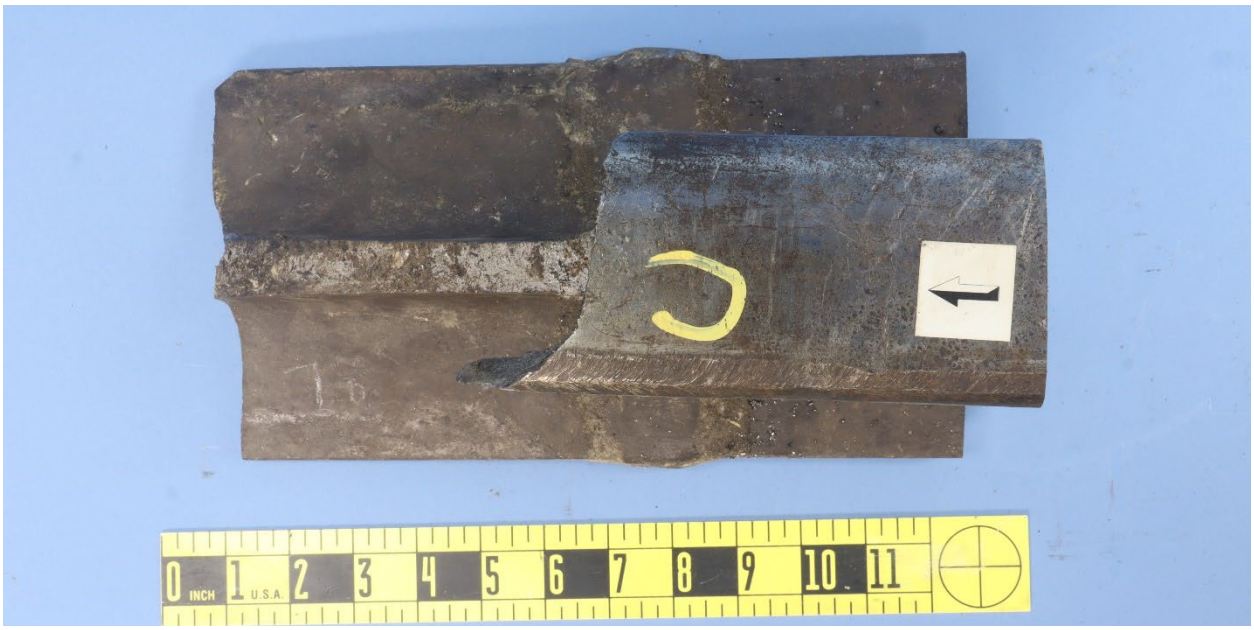

Figure 27. Top down view of the fractured rail with the fractured remnants in place at the time of sectioning.

Figure 28. View of Figure 25 with the head fragment removed and placed upward.

Figure 29. Direct view of the 'C' fracture surface, which both fragments in place.

Figure 30. Cross sections of the rail pieces from either side of the rail, with the newer rail 1 from the A-side of the fracture on the left, and the older rail 2 from the B-side of the fracture on the right.

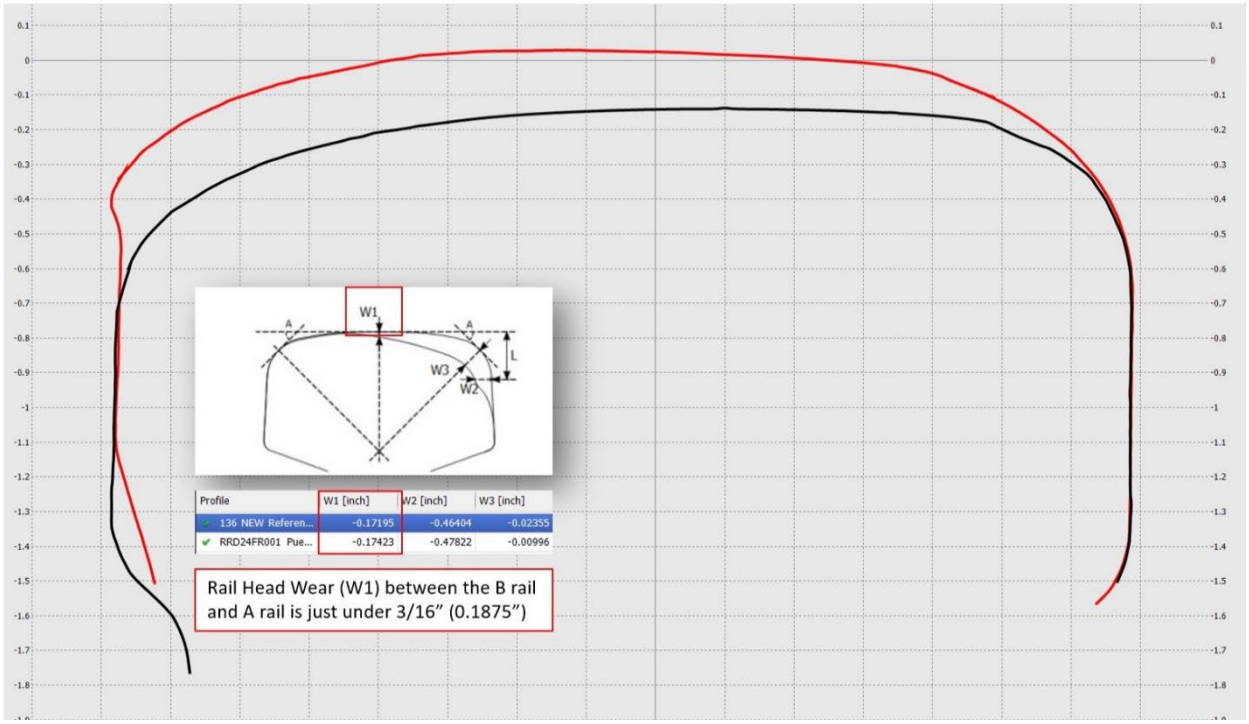

Figure 31. Rail head profile data comparing the A-side rail 1 (black line) and B-side rail 2 (red line) sides of the rail away from the fracture.

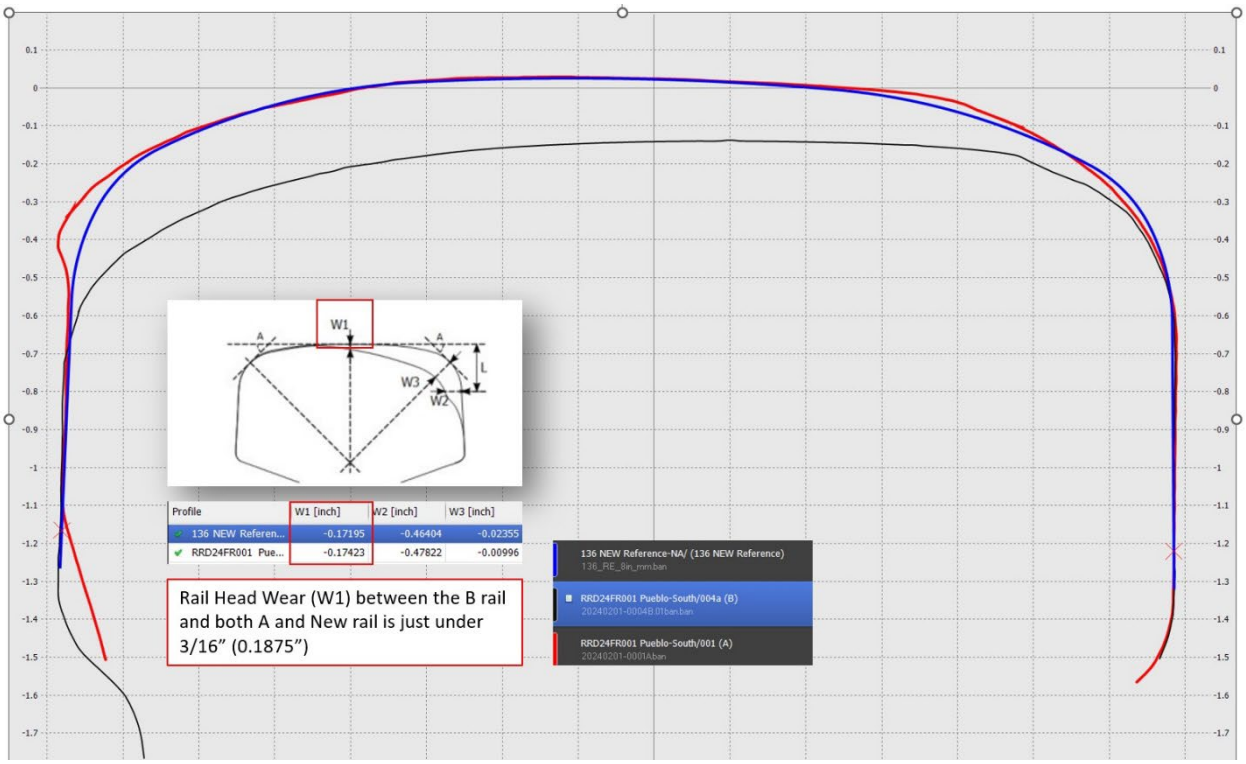

Figure 32. Rail head profile data comparing rail 1 (black line) and rail 2 (red line) profiles measured away from the fracture to an idealized 136-lbs. rail profile (blue).

Figure 33. Longitudinal sections of rail pieces 2 and 1, positioned as sectioned, viewed from the gage side.

Figure 34. Longitudinal sections of rail 2 (left) and rail 1 (right), viewed from the fracture surfaces.

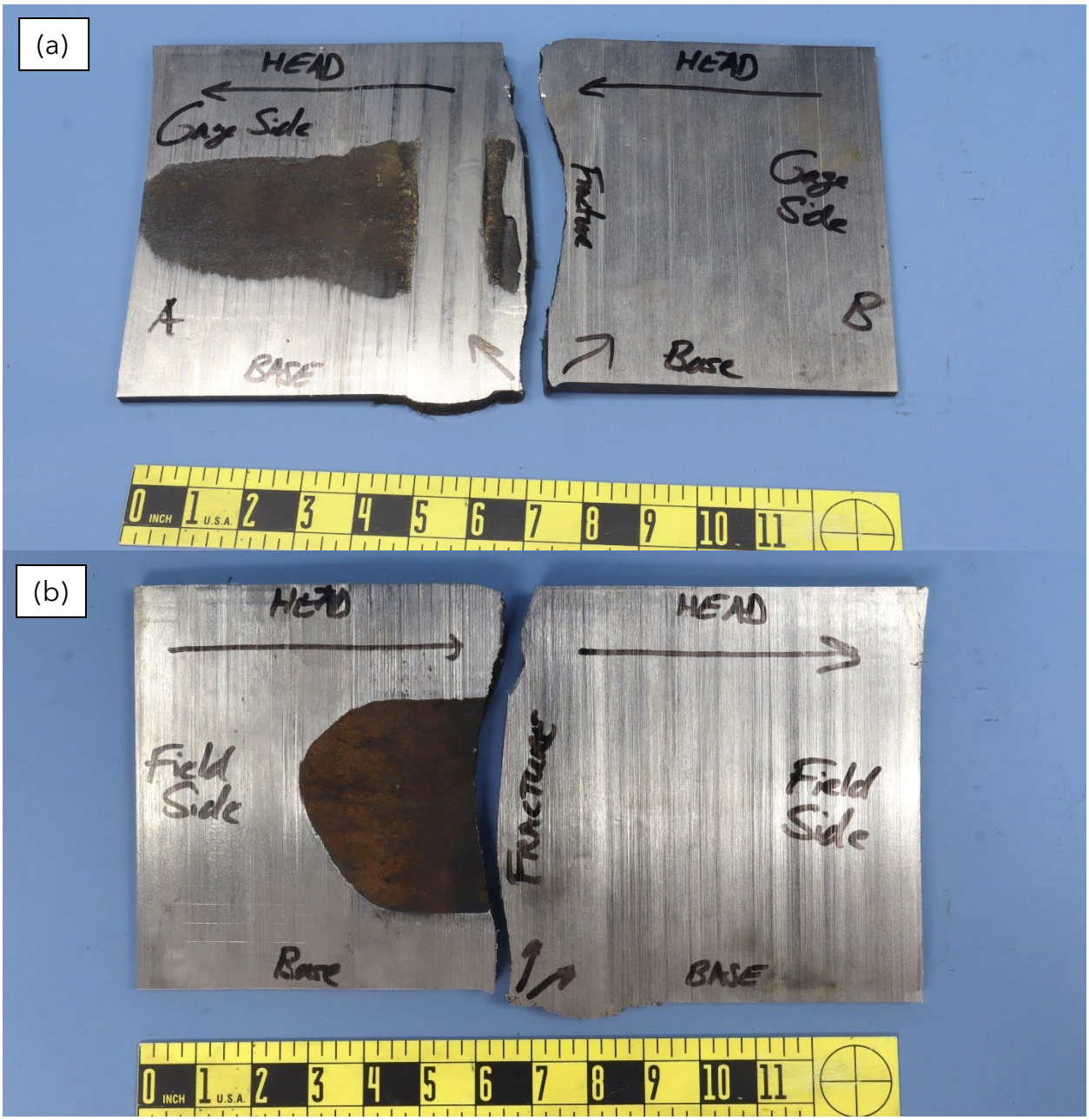

Figure 35. View of the centerline longitudinal sections with the locations of the head and base labeled from (a) the gage side and (b) the field side.

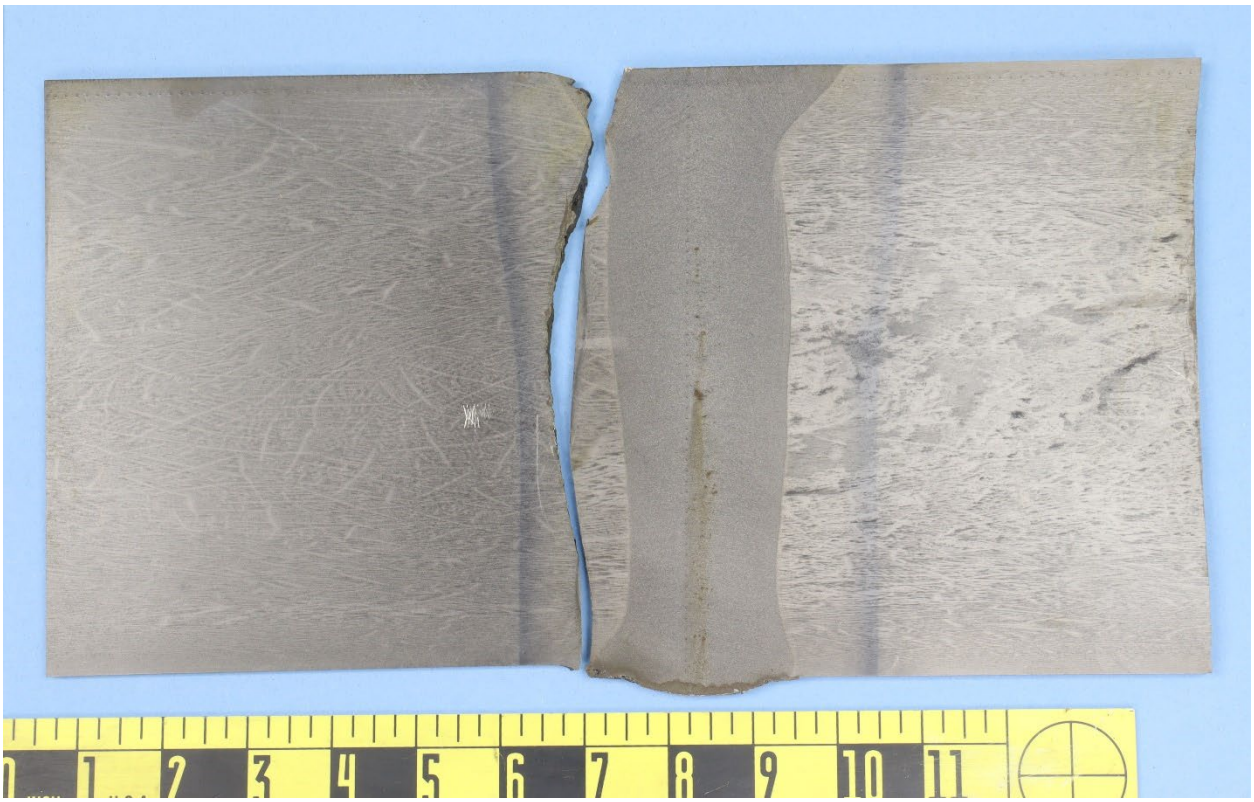

Figure 36. View of the longitudinal section across the weld, after etching.

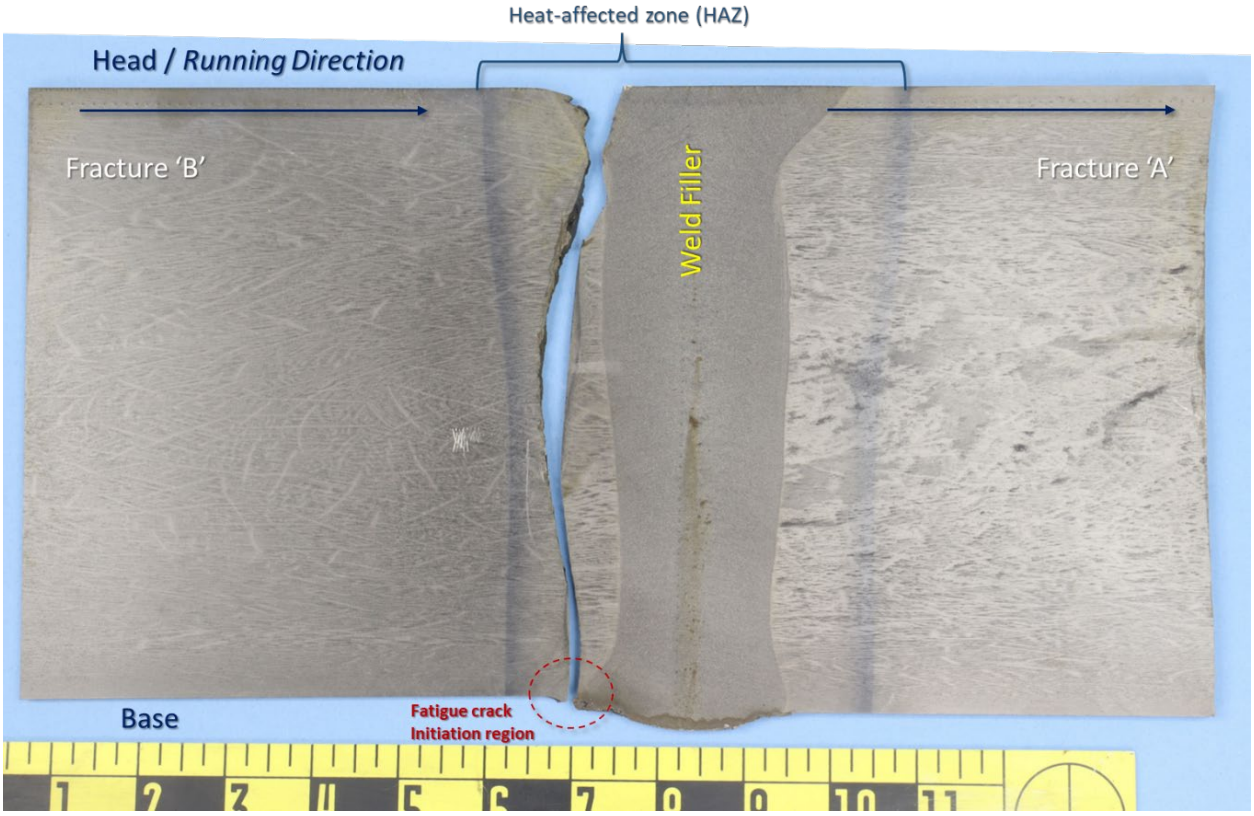

Figure 37. The etched longitudinal section across the weld, annotated.

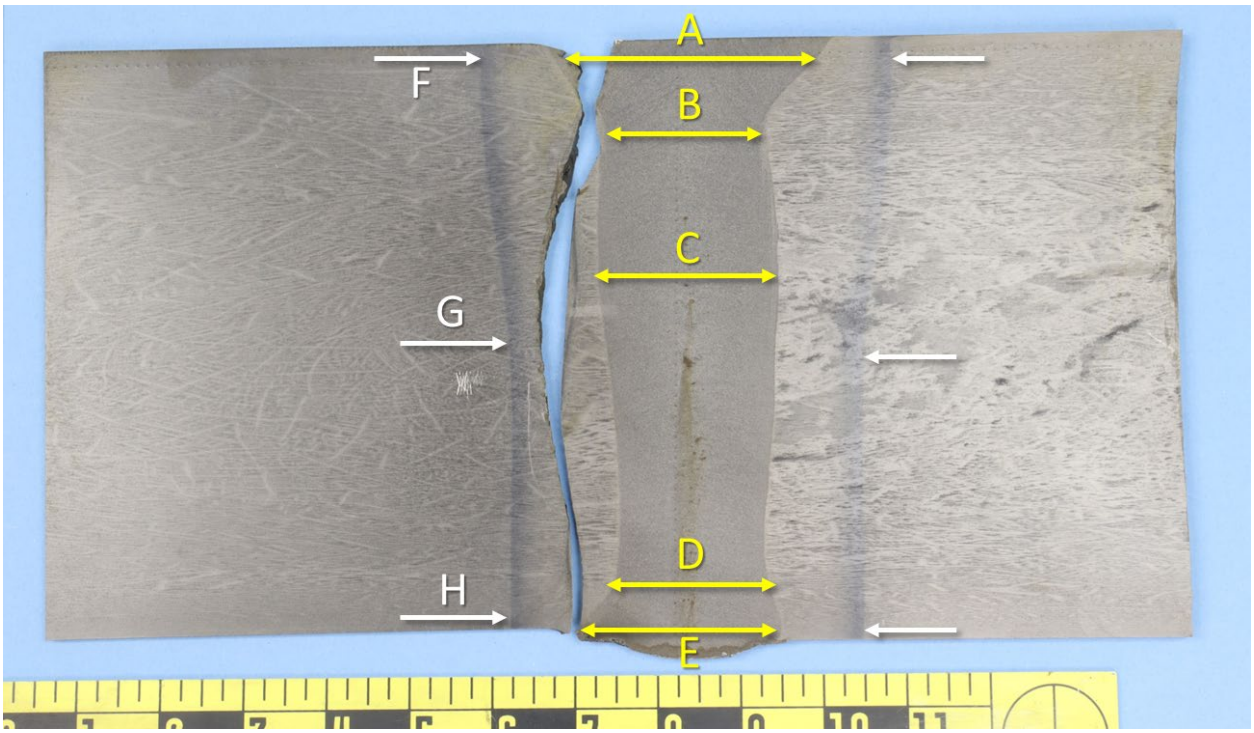

Figure 38. Measurements required in the weld qualification. Data are in Table I.

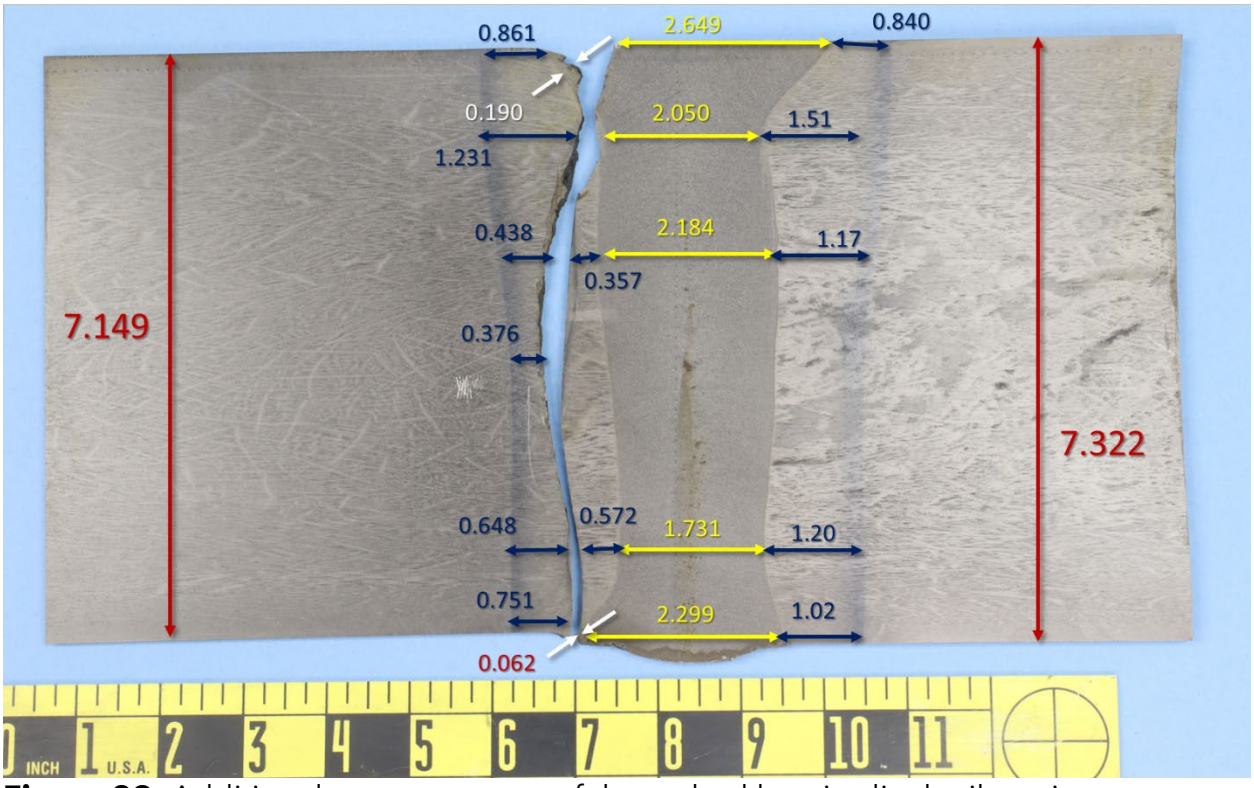

Figure 39. Additional measurements of the etched longitudinal rail sections, annotated on the figure.

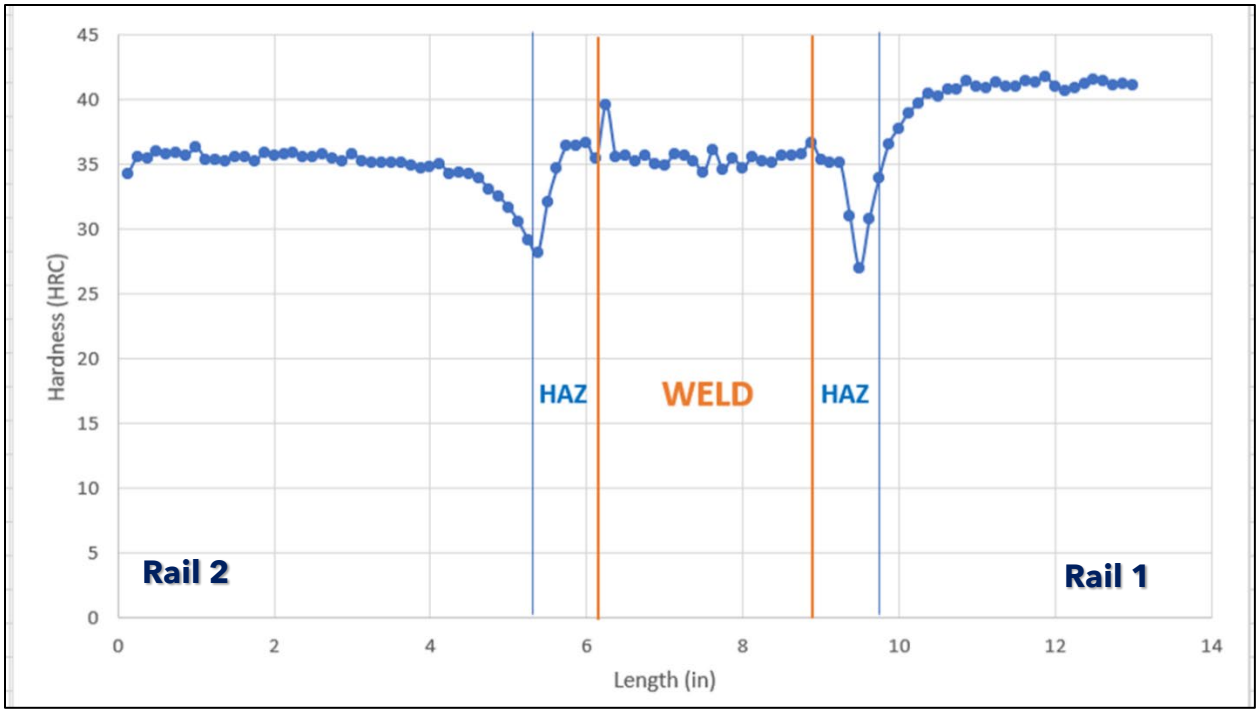

Figure 40. Series of hardness data (in HRC) taken longitudinally across the ground section, with the HAZ and weld areas annotated.

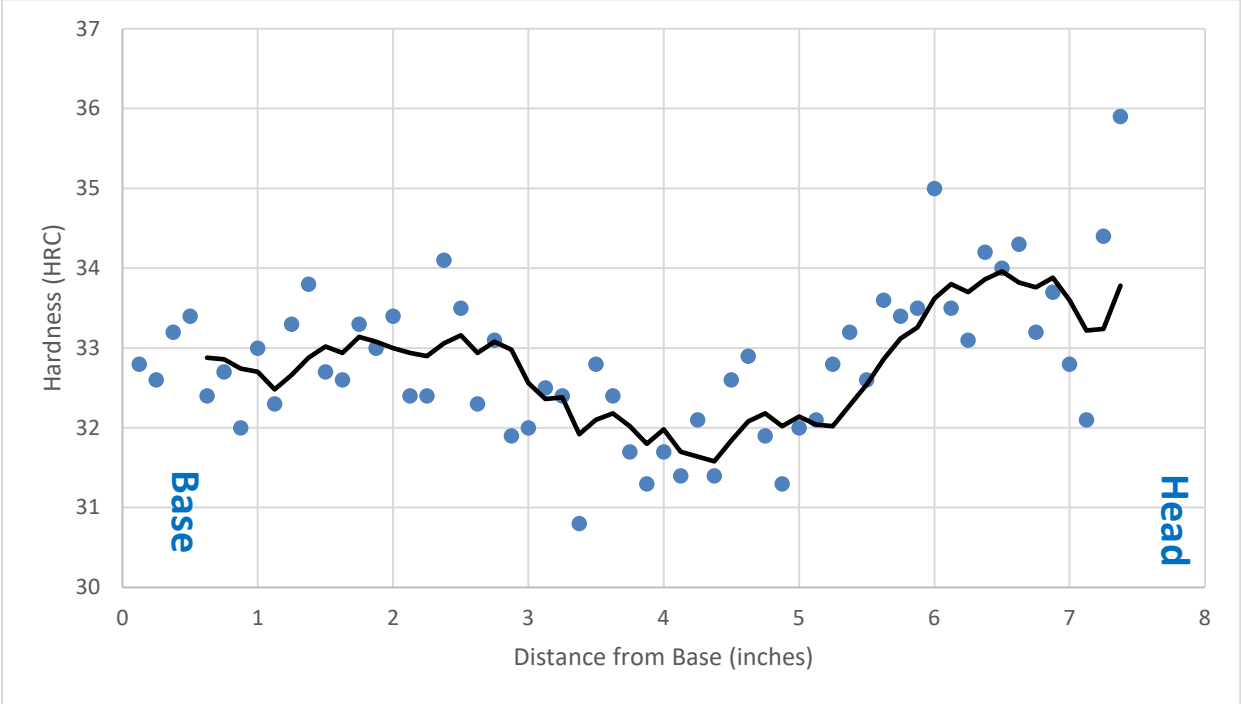

Figure 41. Hardness data (in HRC) taken vertically (transverse) across the Rail 1 from base to head outside the HAZ, with the black line representing a 5-period moving average of the data.

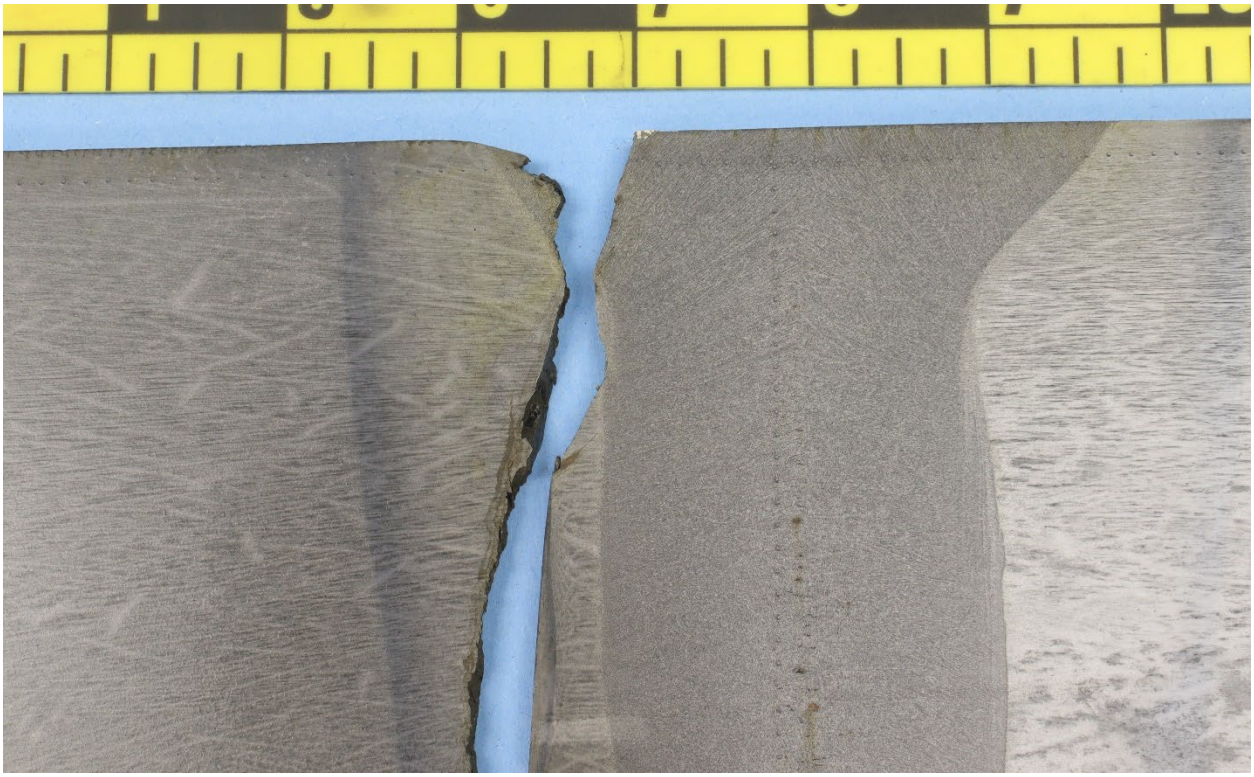

Figure 42. Closer view of the head portion of the etched weld section.

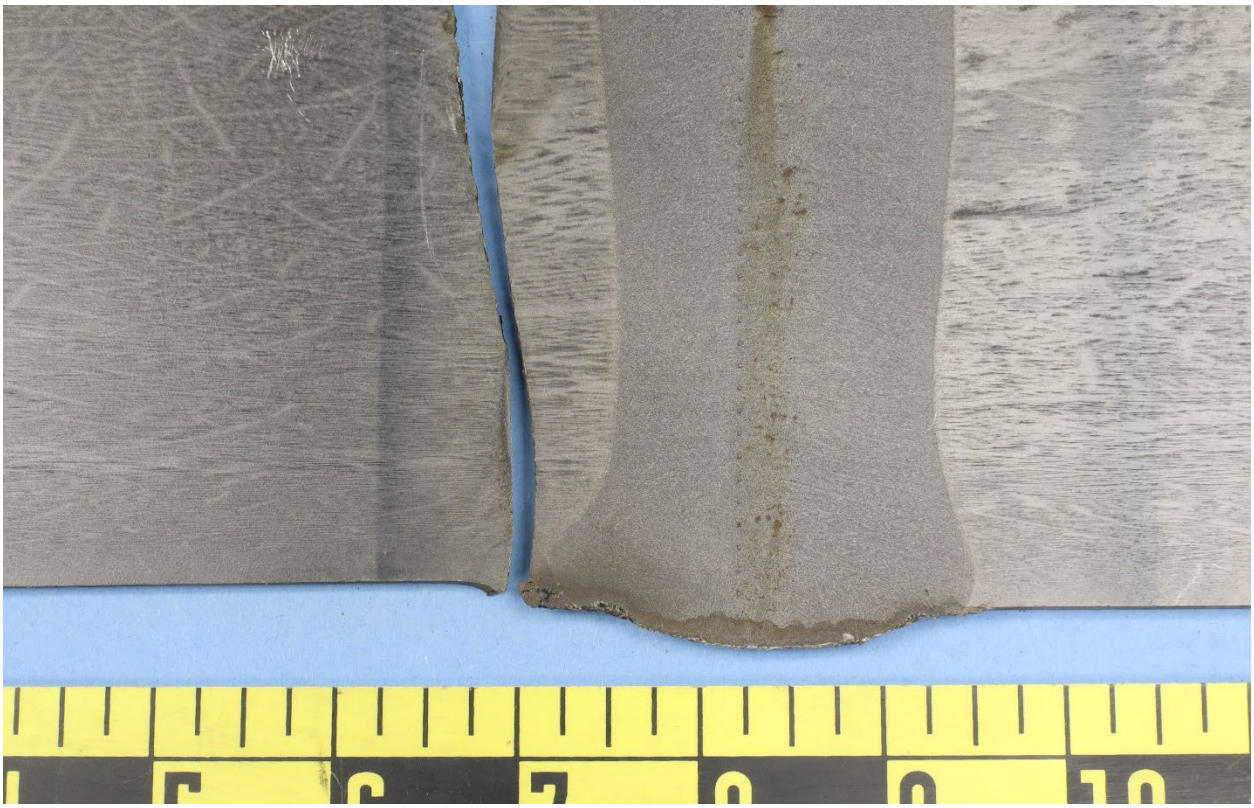

Figure 43. Closer view of the weld on the etched section near the base and the location of fatigue crack initiation.

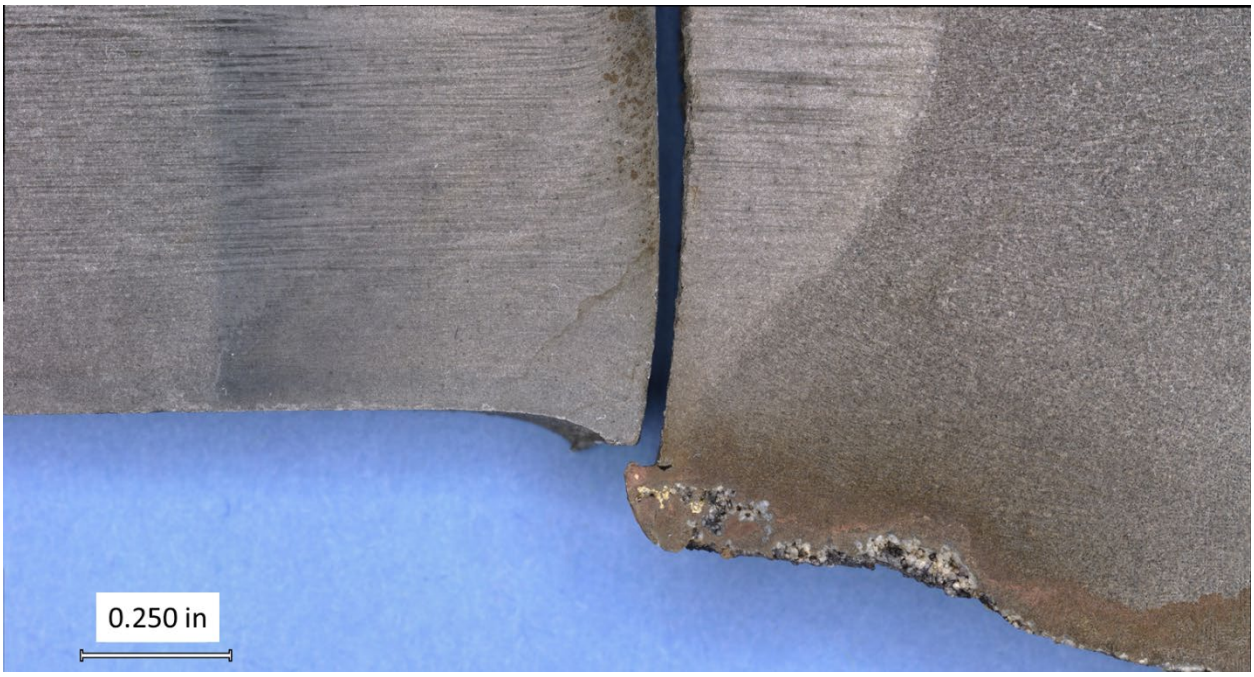

Figure 44. Closer view of the lower portion of the weld in the etched longitudinal section.

Figure 45. Closer view of the section through the fatigue crack initiation site, flash, and lower portion of the weld.

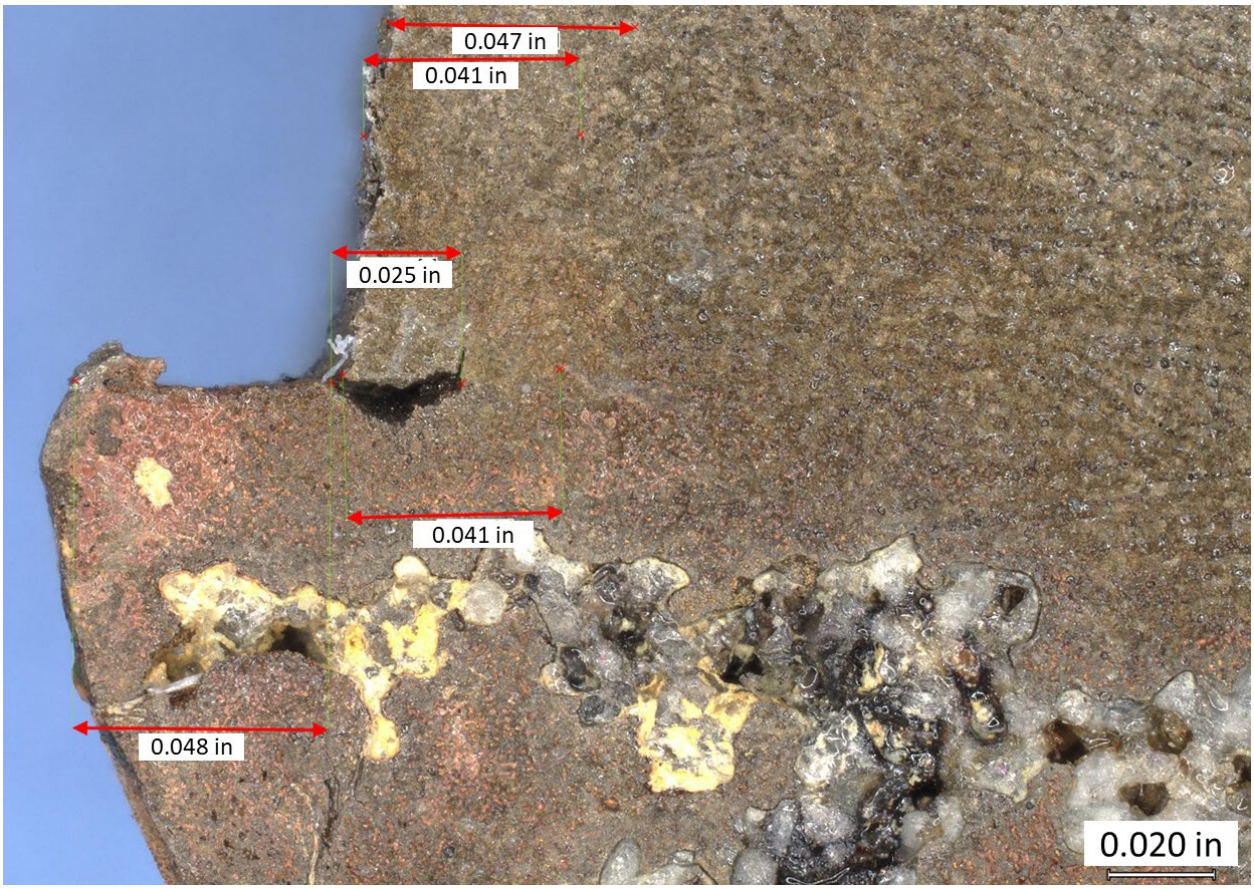

Figure 46. Closer view of the weld and flash side of fracture surface 'A', annotated with measurements.

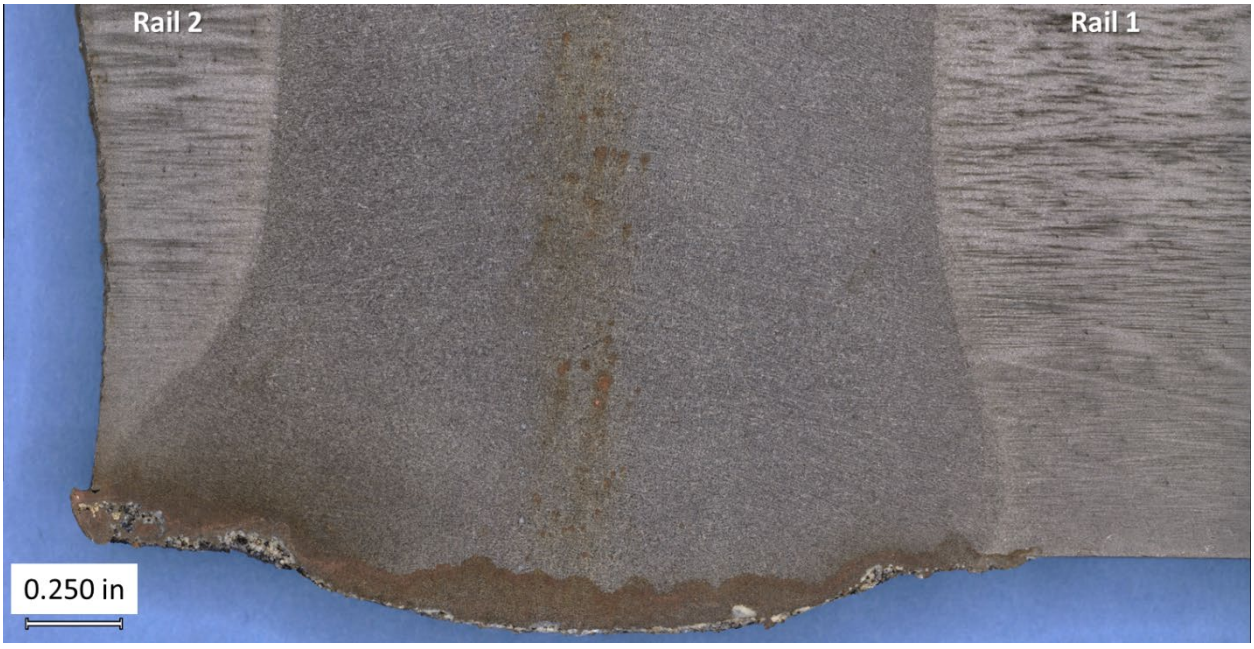

Figure 47. View of the base and lower weld portions in the longitudinal section on the 'A' fracture side.

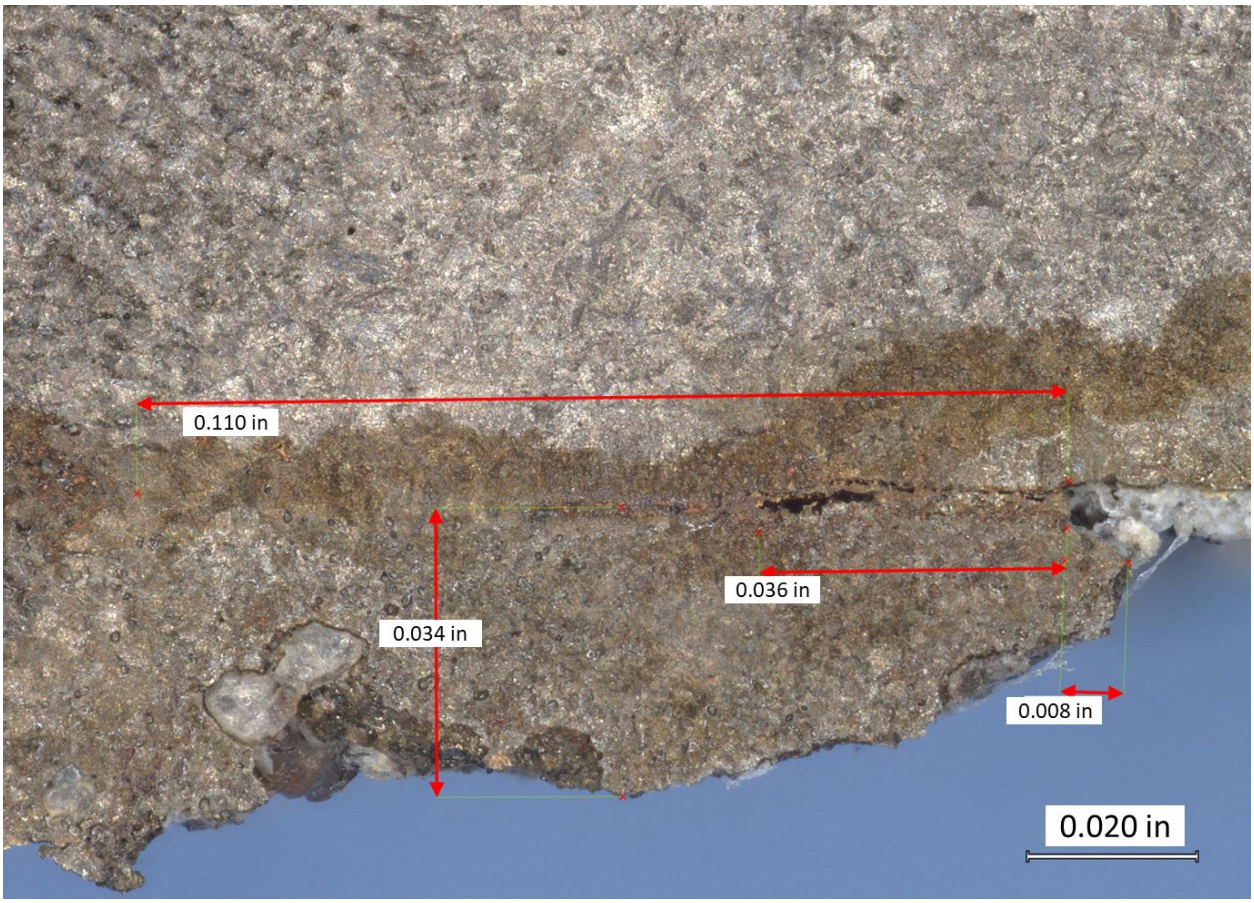

Figure 48. The opposite side of the base and flash on rail 1, showing a horizontal crack between the flash and the rail underside. Various measurements are annotated.

Figure 49. Montage of an additional section of the rail weld base on the 'A' fracture side, after sectioning (mirrors orientation in Figure 47).

Figure 50. BF optical micrograph of the corner of the weld filler and the rail 2 HAZ from the A side rail (~25X, etched 2% Nital).

Figure 51. BF optical micrograph of the corner of the weld filler and base of the rail 1 side (~50X, etched 2% Nital). The darkest areas were artifacts from the etching process.

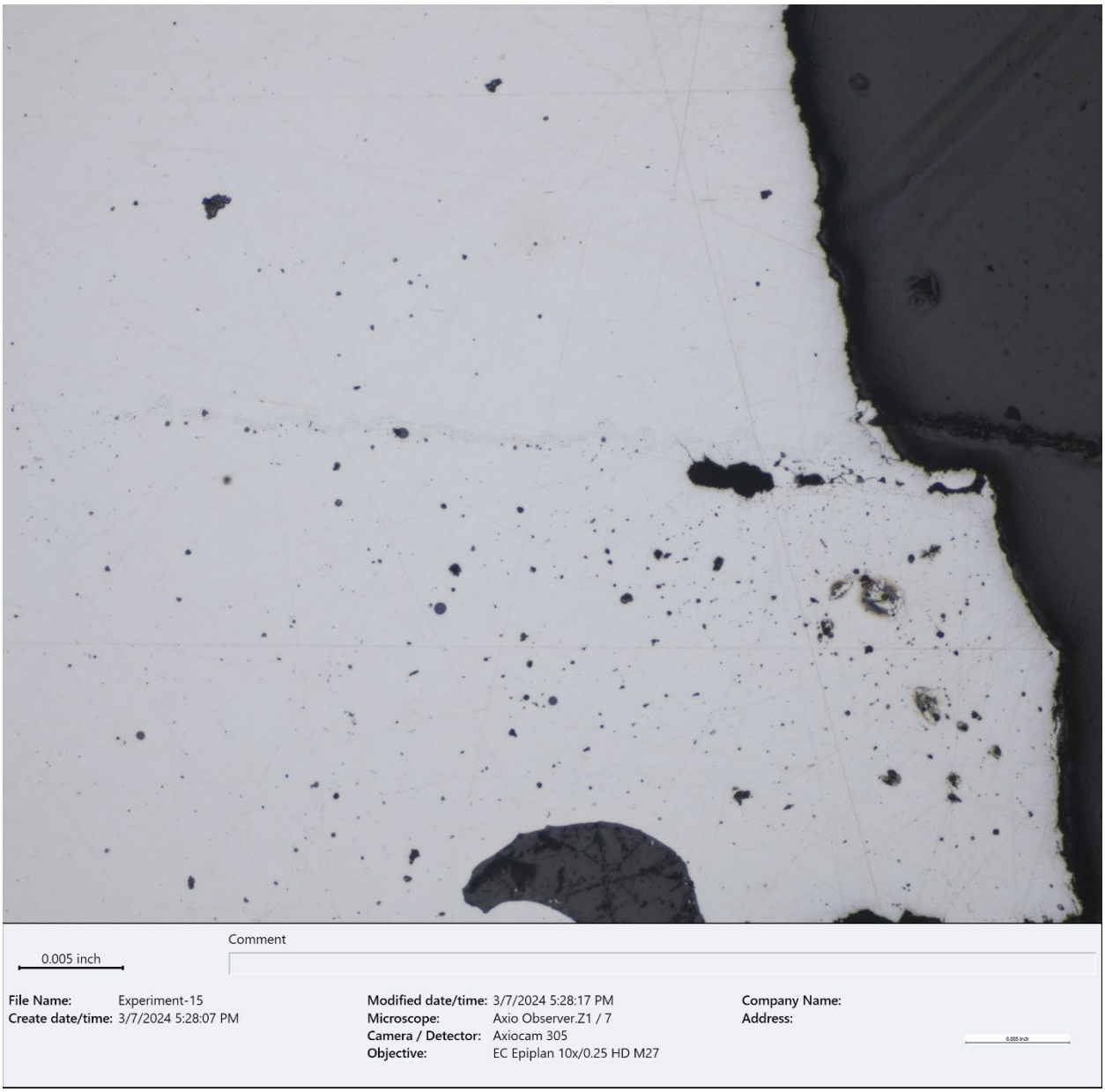

Figure 52. BF optical micrograph of a cross section through the flash and base at the A fracture surface (~100X, as polished).

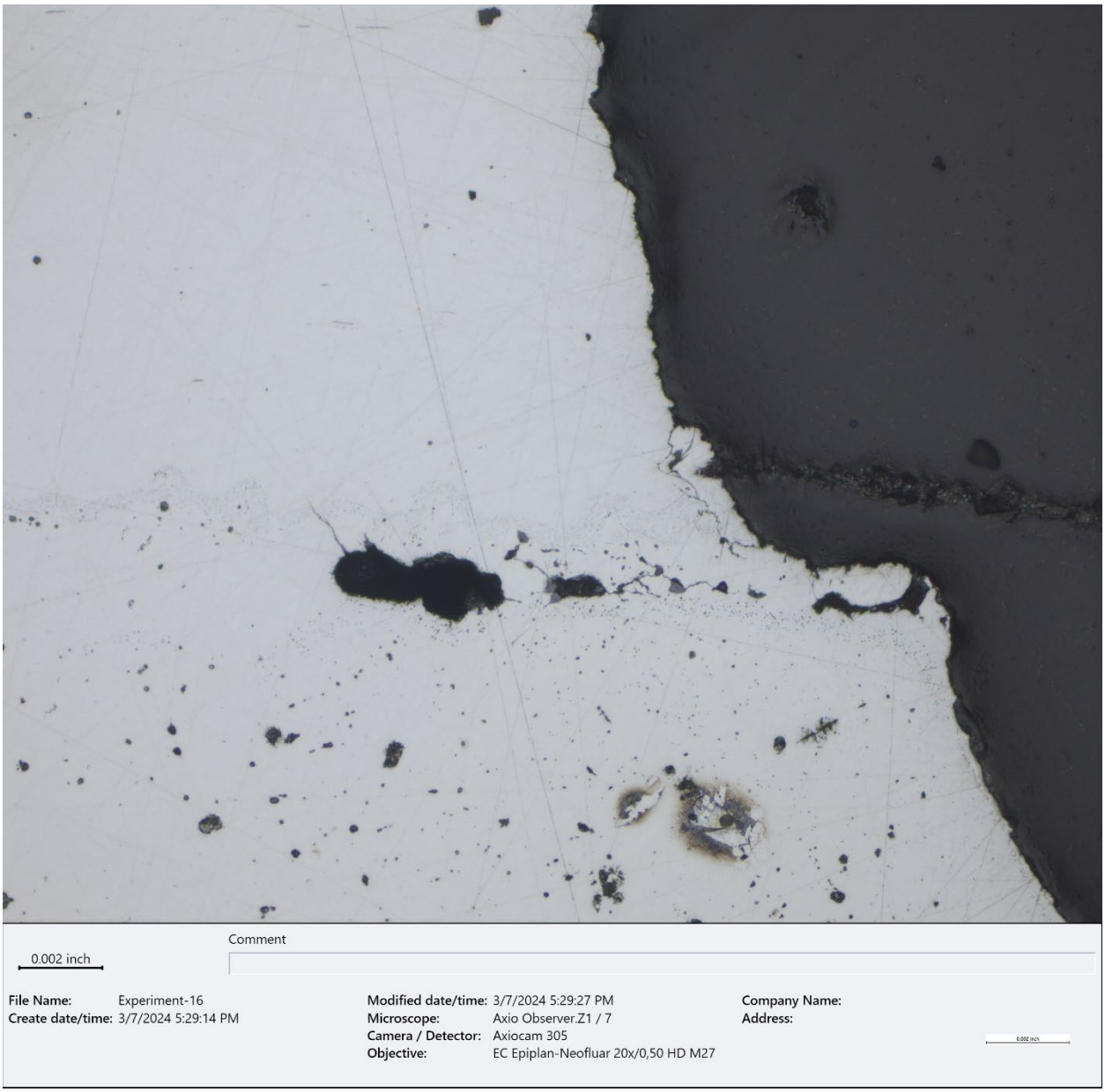

Figure 53. BF optical micrograph of a cross section through the flash and base at the A fracture surface (~200X, as polished).

Figure 54. BF optical micrograph of a cross section through the flash and base at the A fracture surface (~100X, etched 2% Nital).

Figure 55. BF optical micrograph of the interior regions of the porosity and crack between the flash and base at the A fracture surface (~200X, etched 2% Nital).

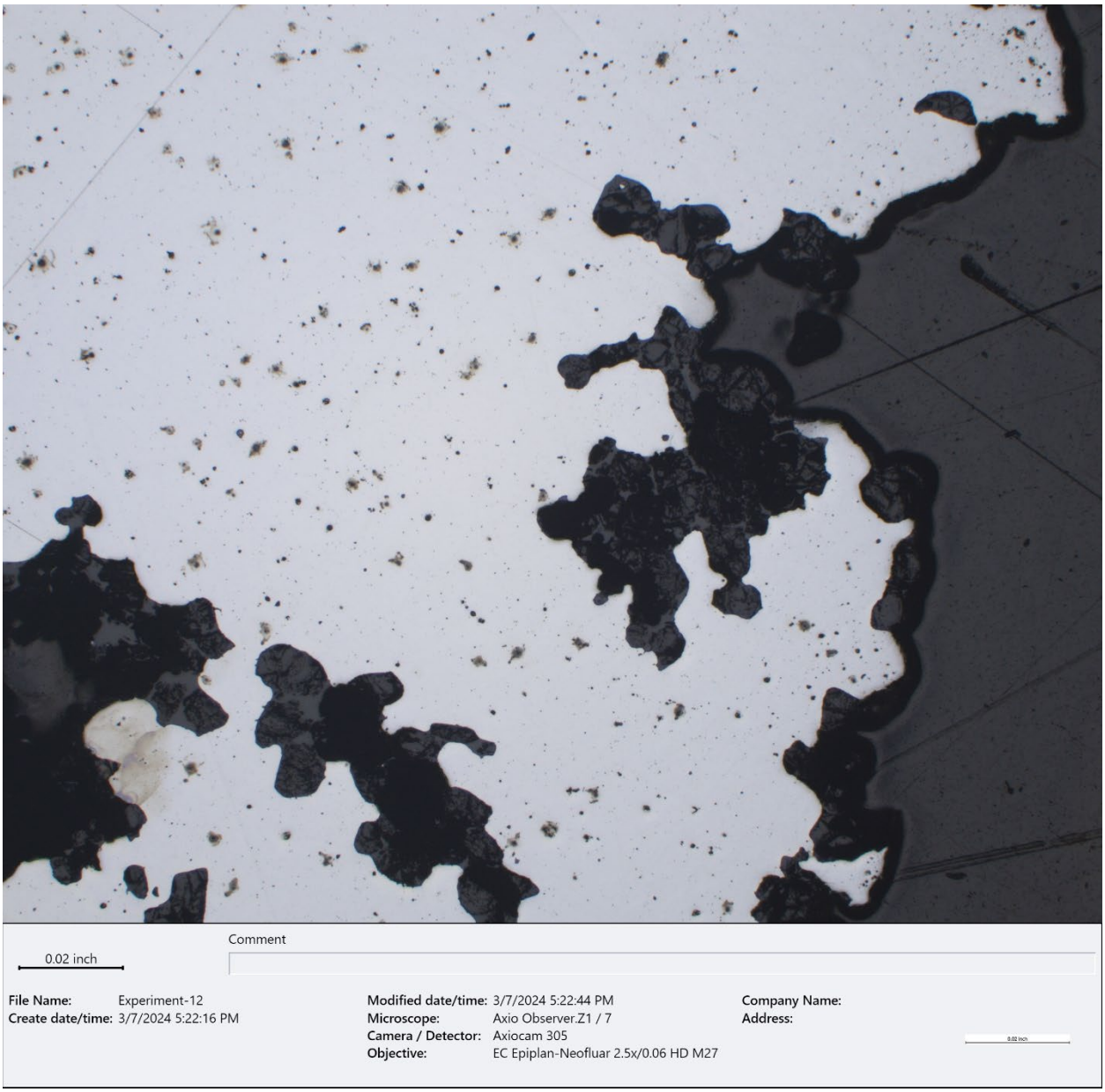

Figure 56. BF optical micrograph of a cross section through the flash at the A fracture surface, showing the porosity and entrained nonmetallic material (~200X, as polished).

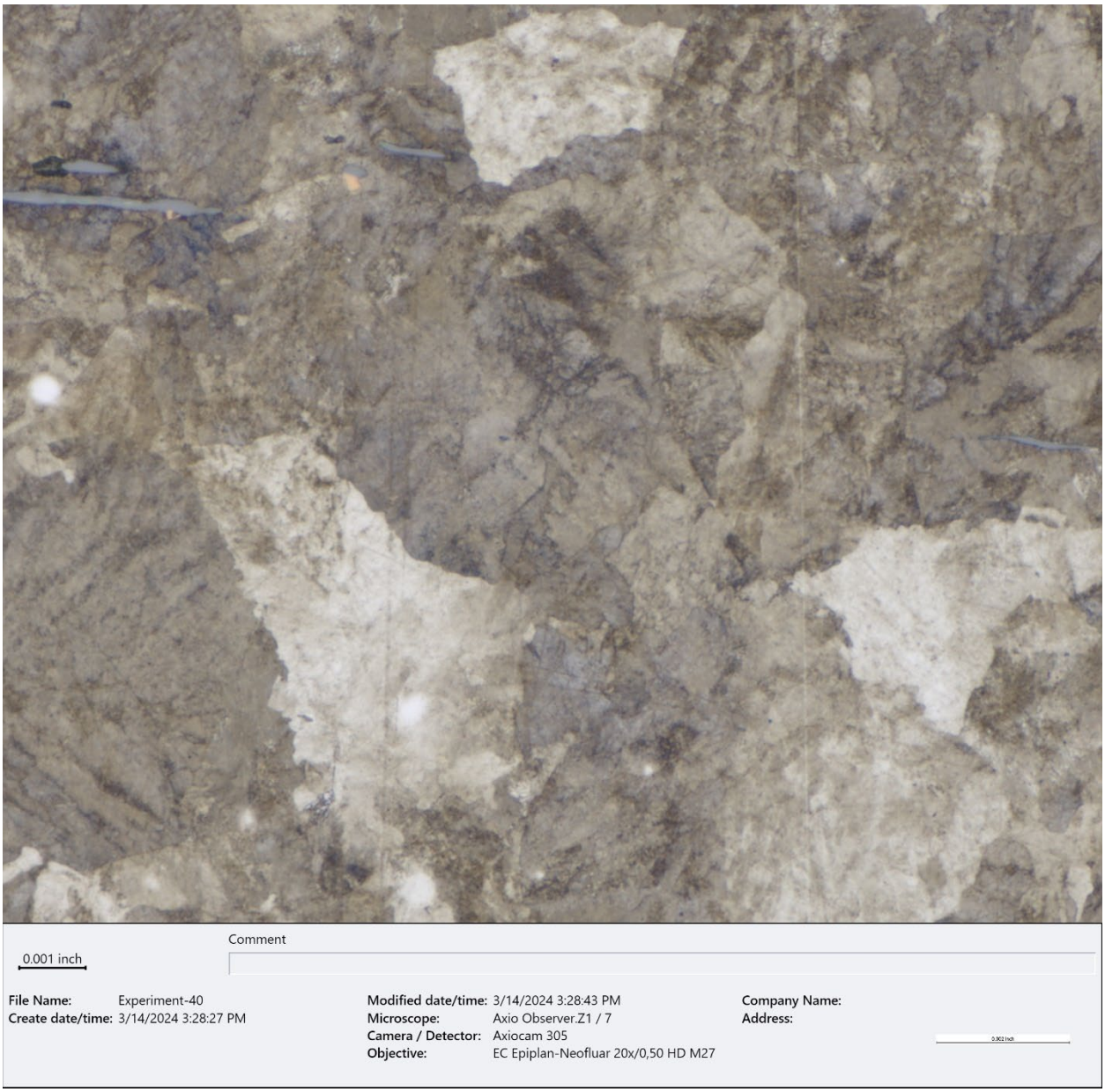

Figure 57. BF optical micrograph of a typical area of the microstructure of rail 2 away from the weld and HAZ (~320X, etched 2% Nital).

Figure 58. BF optical micrograph of a typical area of the interface between the weld filler and the rail 2 material (in the HAZ) (~100X, etched 2% Nital).

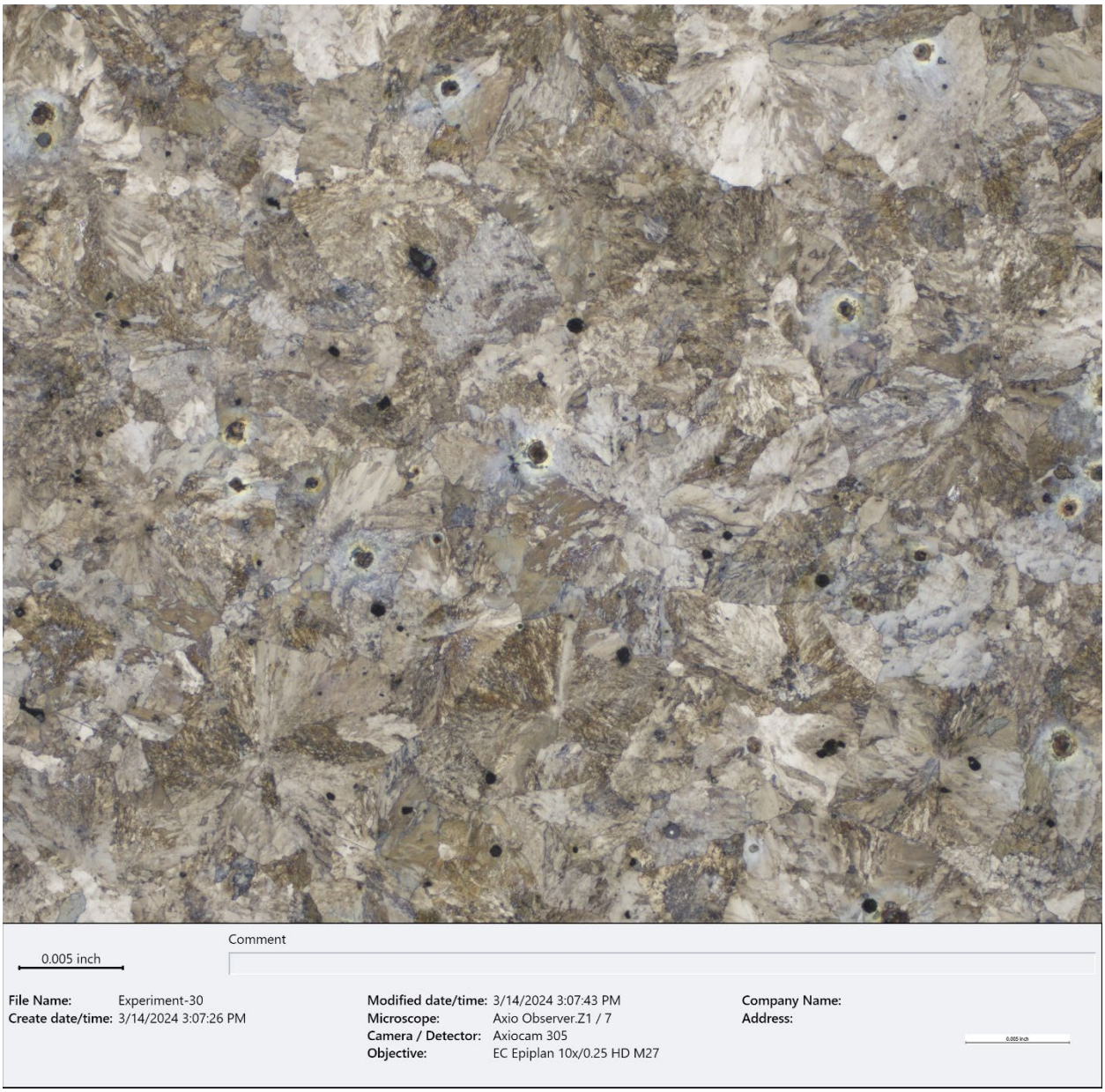

Figure 59. BF optical micrograph of a typical area of the weld filler microstructure in (~100X, etched 2% Nital).

Figure 60. BF optical micrograph of a typical area of the weld filler microstructure, showing lamellar pearlite colonies (~500X, etched 2% Nital).

Figure 61. BF optical micrograph of a typical area of the weld filler near the base showing interdendritic porosity (~100X, etched 2% Nital).

Figure 62. BF optical micrograph of a closer view of an area in Figure 61, showing porosity and pearlitic grains (~200X, etched 2% Nital).